



The role of trace elements in controlling H incorporation in San Carlos olivine

Peter M. E. Tollan^{1,2} · Hugh St. C. O'Neill² · Jörg Hermann¹

Received: 5 July 2018 / Accepted: 3 October 2018
© Springer-Verlag GmbH Germany, part of Springer Nature 2018

Abstract

We conducted a series of hydroxylation experiments using mm-sized cuboids cut from six different crystals of San Carlos olivine with a range of trace-element concentrations. The cuboids were pre-annealed and then hydroxylated under identical conditions, ensuring that variation in the amounts of H incorporated depended only on the compositional variables. The pre-anneal was at 1400 °C, atmospheric pressure and an oxygen fugacity equivalent to $\Delta \log \text{FMQ} + 1$, with the subsequent hydroxylation at 800 °C and 1.5 GPa, for 3 days. Hydrogen was incorporated into all six crystals by the four main substitution mechanisms [Si], [Mg], [Ti] and [triv], with homogeneous H contents in the cores of the crystals, indicating H diffusion rates faster than $10^{-11} \text{ m}^2/\text{s}$. Total H as H_2O in the homogeneous cores calculated by summing all the infrared absorbance bands ranges from 13 to 27 wt. ppm. The total H_2O in the six pre-annealed crystals is poorly correlated with any measured compositional variable. However, when the H_2O associated with individual infrared bands is compared, clear trends emerge. The intensity of absorption bands at 3572 and 3525 cm^{-1} are strongly correlated with Ti concentrations, whose range in the six crystals exceeds an order of magnitude. Bands between 3400 and 3300 cm^{-1} , correlate negatively with Na^+ , but are positively correlated with the difference between molar Cr^{3+} and Na^+ . This highlights a previously unrecognised role for Na in suppressing H incorporation in natural olivines. The results confirm the important role that the trace constituents of olivine play in H incorporation. Two of these trace elements, Na and Ti, tend to be similarly enriched or depleted by partial melting or metasomatism of the mantle, but have opposite effects on H incorporation, with Ti enhancing it but Na suppressing it. Models estimating the effect of H in olivine on mantle rheology must, therefore, consider carefully the availability of these trace elements.

Keywords Water · Olivine · Mantle · Point defect · Trace element · Diffusion

Introduction

Hydrogen attached to oxygen anions to form hydroxyl-bearing point defects is a trace constituent of terrestrial olivine, with concentrations measured in exhumed mantle fragments typically occurring in the range < 1 to 100 wt.

Communicated by Hans Keppler.

Electronic supplementary material The online version of this article (<https://doi.org/10.1007/s00410-018-1517-7>) contains supplementary material, which is available to authorized users.

✉ Peter M. E. Tollan
peter.tollan@geo.unibe.ch

¹ Institut für Geologie, Universität Bern, Bern, Switzerland

² Research School of Earth Sciences, The Australian National University, Canberra, Australia

ppm as the oxide component H_2O (Demouchy and Bolfan-Casanova 2016). Despite such low concentrations, the presence of H has significant effects on the physical properties of olivine, and thus exerts substantial control on the behaviour of the upper mantle. Most notably, addition of water results in increased strain rate (Mackwell et al. 1985; Mei and Kohlstedt 2000; Faul et al. 2016), electrical conductivity (Karato 1990; Yoshino et al. 2006), solid-state chemical diffusion rates (Wang et al. 2004; Demouchy et al. 2007), and decreased solidus temperature (Kóvacs et al. 2012).

Determining the water content of the mantle from natural samples is limited in two ways. First, xenoliths and peridotite massifs typically only sample the uppermost mantle, hence biasing heavily the view of the mantle as a whole. Second, the rapid diffusivity of H through the olivine lattice means that original concentrations are often heavily modified by diffusive loss under the condition of significantly lowered

water fugacity imposed during magmatic ascent (Demouchy et al. 2006; Peslier et al. 2008; Denis et al. 2013; Padrón-Navarta et al. 2014; Tollan et al. 2015). In light of this, a number of experimental studies have been conducted to develop predictive models which relate the capacity to store water with different system variables thought to exert influence (Bai and Kohlstedt 1993; Matveev et al. 2001; Lemaire et al. 2004; Zhao et al. 2004; Mosenfelder et al. 2006; Smyth et al. 2006; Grant et al. 2007a, b; Bali et al. 2008; Withers and Hirschmann 2008; Gaetani et al. 2014; Yang 2016; Tollan et al. 2017a). These studies have shown that mantle olivine can contain orders of magnitude more water than revealed through direct measurement of naturally exhumed olivine, particularly at higher pressures and water activities where point defects with a higher molar concentration of H are stabilised compared to those under typical conditions in the shallow lithospheric mantle (Kohlstedt et al. 1996; Smyth et al. 2006; Padrón-Navarta and Hermann 2017; Tollan et al. 2017a).

A prevailing question is the structure of the point defects containing H. It is generally agreed that in olivine H substitutes into vacant tetrahedral or octahedral sites to charge balance neighbouring O sites forming O–H groups (Matveev et al. 2001; Lemaire et al. 2004; Smyth et al. 2006) although interstitially-located H may also contribute to the total H budget (Balan et al. 2014). These O–H groups are infrared active, with the O–H stretching frequency dependent on the local bonding environment. Hence, Fourier transform infrared (FTIR) spectroscopy, supported by theoretical calculations of the free energies of different point defect configurations (e.g. Walker et al. 2007), can be a powerful tool to deduce the relative proportions of these hydrous defects and how they contribute to the total mantle water budget. Applying FTIR spectroscopy to natural olivines has shown that the infrared absorption bands of olivine in simple synthetic systems poorly replicate those in the natural system, indicating that some aspect of the O–H bonding environment in natural olivines is different (Berry et al. 2005). Early experimental work on H₂O incorporation in olivine did not consider the possibility that minor or trace elements (excepting Fe³⁺) would play a significant role, despite using natural materials, such as San Carlos olivine, containing amounts of these elements that are typical of mantle olivines. The experimental studies of Berry et al. (2005) and Berry et al. (2007a, b) showed that this was not the case. The infrared spectra of the very small amounts of H₂O (< 1 ppm) naturally occurring in San Carlos olivine and similar olivine from spinel peridotite xenoliths analysed by Miller et al. (1987) was due to a substitution mechanism involving Ti. Moreover, the infrared fingerprint of this substitution mechanism was prominent in the infrared spectra of experimentally hydroxylated San Carlos olivines in the previous experimental work (Bai and Kohlstedt 1992, 1993; Mackwell and; Kohlstedt 1990;

Kohlstedt and Mackwell 1998). In fact, Berry et al. (2005, 2007a, b) demonstrated that there were two entirely different substitution mechanisms mediated by trace elements, one with Ti, and the other with those trivalent cations that substitute into the octahedrally coordinated crystallographic sites of olivine, charge-balanced by octahedral site vacancies. In theory this would permit the infrared fingerprint of natural olivines to be linked to the chemistry and redox state of the geochemical environment in which they last equilibrated. A number of subsequent experimental studies have shown similar links (Grant et al. 2007b; Férot and Bolfan-Casanova 2012; Padrón-Navarta et al. 2014; Jollands et al. 2016; Tollan et al. 2017a), backed up by theoretical calculations (Walker et al. 2007; Balan et al. 2011; Blanchard et al. 2017). In the natural environment, Schmädicke et al. (2013), Shen et al. (2014) and Tollan et al. (2015) all put forward empirical evidence that the availability of Ti and the trivalent cations Cr³⁺ and Fe³⁺ can have significant influence on water incorporation in upper mantle olivine. Against this, Demouchy and Bolfan-Casanova (2016) summarise that, based on existing literature data, for typical mantle olivine compositions, there is little evidence for significant coupled substitution of water with Ti. Experimental studies of Smyth et al. (2006), Withers and Hirschmann (2008), Férot and Bolfan-Casanova (2012) and Gaetani et al. (2014) concluded likewise that trace element-related defects do not play a significant role in water incorporation in olivine at the compositions and conditions investigated.

In this study, we address this conundrum through experiments on a selection of six natural San Carlos olivines that possess a range of trace-element compositions representative of the upper mantle. San Carlos olivines were chosen not only because their gem quality makes them suitable for experiments using infra-red spectroscopy, but also because individual crystal are remarkably homogeneous in trace elements as well as major elements, despite the large differences in the concentrations of many trace elements between different crystals (see below). By keeping all other variables constant we identify the chemical species that are significant to water incorporation in typical upper mantle olivine. We then assess the implications of these relationships for predicting the water storage capacity and content of the mantle in different settings.

Methods

Experimental strategy

There are two fundamentally different experimental approaches to investigate H₂O incorporation in nominally anhydrous minerals such as olivine, which we have designated “G” (global equilibrium) and “M” (metastable

equilibrium) experiments (Tollan et al. 2017a). With the former, the aim is to achieve complete equilibrium within the thermodynamic environment of the experiment. To do this, the olivine is grown during the experiment from natural or synthetic starting materials, resulting in crystals that have the equilibrium stoichiometry, trace-element contents and other aspects of their point-defect structure at the experimentally imposed conditions (e.g., Bai and Kohlstedt 1992; Matveev et al. 2001; Berry et al. 2005; Grant et al. 2007a; Withers and Hirschmann 2008; Withers et al. 2011; Férot and Bolfan-Casanova 2012; Padrón-Navarta et al. 2014). The “M” type of experiment uses the faster diffusion of H compared to other species to introduce H into pre-existing crystals, preserving some characteristics of those crystals, particularly their major- and trace-element compositions. These M-type experiments have the experimental advantage that large gem-quality crystals of natural mantle olivine can be used, allowing polarized transmitted light infrared spectra to be collected along known crystallographic axes. Such experiments may be further classified into two subgroups: M_2 experiments hydroxylate the crystals at relatively low temperatures, seeking to decorate existing point defects with H, preserving a memory of their last equilibration environment as regards T, P, fO_2 and $a(SiO_2)$ as far as possible, whereas M_1 experiments accept that aspects of the point-defect structure of the crystal will change in response to the T, P, fO_2 and $a(SiO_2)$ of the hydroxylation. Probably most M-type experiments fall between these two ideals, but the experiments of Bai and Kohlstedt (1992), Zhao et al. (2004), Grant et al. (2007b) and Gaetani et al. (2014) may be considered as M_1 , whereas those of Bai and Kohlstedt (1993) and Jollands et al. (2016) are M_2 . The M_2 approach is particularly informative about olivine point-defect chemistry when used in a two-stage experiment, in which the point-defect structure of the crystal is first imposed by annealing at known T, P, fO_2 and $a(SiO_2)$, with the subsequent hydroxylation stage decorating this imposed point-defect structure with H for fingerprinting by infra-red spectroscopy.

Here, we use the two-stage M_2 approach because it allows us to use gem-quality single crystals of olivine to obtain the polarized infra-red spectra on oriented single crystals that can be deconvoluted to quantify the different substitution mechanisms, while also isolating the variables of composition from the extensive thermodynamic variables (T, P, fO_2 and $aSiO_2$). Whilst such an approach is highly useful for deducing the substitution mechanisms for the specific crystal compositions and metastable equilibrium conditions (imposed here during the initial pre-anneal), in nature the greater timescales and strain rates will result in evolution towards a global equilibrium state. Hence, it is important to note that our experimental study here is not an attempt to

determine the global equilibrium storage capacity of water in the upper mantle, merely to establish the key substitution mechanisms which are operating.

Crystal selection and preparation

Crystals were selected from gem-quality San Carlos olivines of the Cr-diopside suite (Wilshire and Shervais 1975), all bearing similar form and colour. Twenty-two crystals were mounted in epoxy resin and polished to expose a small area large enough for LA-ICP-MS analysis. Once all crystals were measured and the results compiled, the crystals were removed from the resin and six compositionally distinct crystals of sufficient size and free of any obvious fractures were selected for the experimental study. These crystals were then cut using a 150 μm diamond saw blade along principle crystallographic axes, recognised through optical microscopy, to produce cuboids with approximate dimensions $1.5 \times 1.5 \times 1.3$ mm. The maximum deviation from each principle axis introduced during this process is estimated to be approximately 10° .

Pre-anneal

The cuboids were annealed at elevated temperature and oxygen fugacity in a 1-atm furnace prior to hydroxylation to equilibrate each crystal at identical conditions, and to increase the capacity for water incorporation (Bai and Kohlstedt 1993). Cuboids from each crystal were packed in individual platinum capsules with San Carlos olivine-orthopyroxene powder and heated at 1400 $^\circ\text{C}$ for 24 h, sufficient for complete thermodynamic equilibrium of intrinsic point defects (Bai and Kohlstedt 1993; Wanamaker 1994). Oxygen fugacity was fixed through a mixture of CO and CO_2 with 2.0% CO to give a condition equivalent to one log unit above the fayalite-magnetite-quartz buffer. This choice of slightly elevated oxygen fugacity results in relatively high $Fe^{3+}/\Sigma Fe$ and $Cr^{3+}/\Sigma Cr$, conducive to hydrogen incorporation, as discussed later. After 24 h, the capsules were dropped onto the steel ball valve that closes the bottom of the furnace, resulting in rapid quenching to ambient temperature without oxidation or cracking. The cuboids were then separated from the sintered matrix and examined by FTIR to confirm the absence of detectable OH.

Hydroxylation

The cuboids were hydroxylated in a 5/8" piston cylinder at 1.5 GPa and 800 $^\circ\text{C}$ for 72 h. The fugacity of pure H_2O (fH_2O°) under these conditions is 48.4 kb from the equation of state of Pitzer and Sterner (1994), but this is reduced by a few percent due to H_2 and dissolved SiO_2 and other components. The assembly design consists of a silver capsule

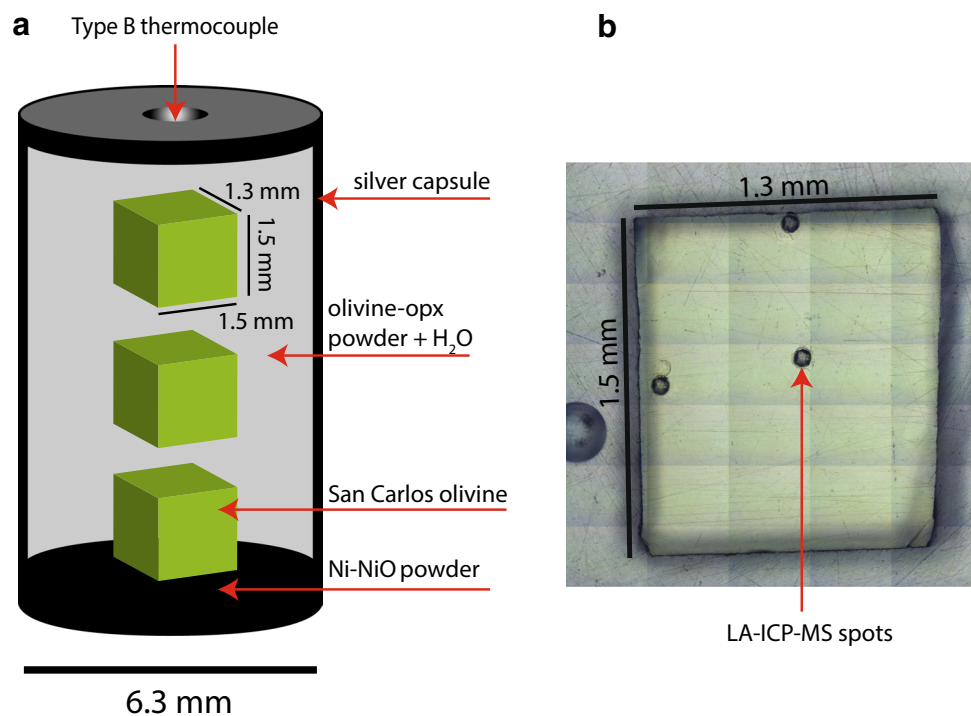
6.3 mm in diameter, packed first with a layer of Ni-NiO powder and subsequently with three olivine cuboids, each from a different crystal, surrounded by San Carlos olivine-orthopyroxene powder (Fig. 1). Buffering silica activity and oxygen fugacity served to ensure that these parameters were consistent between each experiment, however, based on a series of additional experiments, which form part of another ongoing study, the choice of buffering powders has no impact on the intrinsic defect structure or hydroxylation process at such a low temperature, given the duration of the experiment. Importantly, the powders also provide a solid medium to prevent cracking and breakage of the cuboids. Seven drops of distilled water (~27–29 μg) were added using a 5 μl micro-pipette, with the capsule then immediately cold-sealed using a swaging tool, which greatly reduces the chance of losing water at the start of the experiment (Hack and Mavrogenes 2006). The capsule was then inserted into the pressure assembly, surrounded by sleeves of graphite and salt and capped at each end with MgO. Temperature was monitored with a type B thermocouple, sheathed by mullite and inserted through the MgO cap so as to be directly in contact with the lid of the silver capsule. Due to the high conductivity of silver, thermal gradients are expected to be small, confirmed by repeat experiments with cuboids in different positions within the capsule, which resulted in nearly identical results. Pressure and temperature were increased such as to follow approximately the water isochore, thus minimising the risk of the cuboids cracking and fracturing (Jollands et al. 2016). After 72 h, the experiment was

quenched by turning off the power. The capsule was pierced with a drill bit to inspect for free water, confirming the experiment had not suffered any water-leakage during the run. The crystals were then removed and prepared for FTIR analysis.

Mounting and FTIR analysis

Once extracted from the capsule, the cuboids were orientated perpendicular to the *b* axis by FTIR and set in epoxy such that the *a* and *c* axes would be measurable after polishing. Absorption along the unmeasured *b* axis is only a small fraction of total absorption and, therefore, we have followed recent workers in not routinely measuring this absorption (e.g., Demouchy et al. 2016). Once hardened, the epoxy was ground down to produce a doubly polished wafer approximately 600–800 μm thick. The samples were first measured by FTIR spectroscopy at the Research School of Earth Sciences (RSES), The Australian National University using a Bruker Hyperion 1000 microscope attached to a Bruker Tensor 27 FTIR spectrometer equipped with a liquid nitrogen-cooled mercury cadmium telluride detector, global light source, wire-grid polariser and KBr beamsplitter. Further measurements were collected at the Institut für Geologie, Universität Bern using a Bruker Hyperion 3000 microscope attached to a Bruker Tensor II FTIR spectrometer with identical technical specifications as the instrument at RSES. Spectra were collected in transition mode using polarised light and consisted of a total of 64 scans per measurement at

Fig. 1 **a** Experimental design for the hydroxylation of the San Carlos cubes. Experiments were performed under identical conditions in each case (800 $^{\circ}\text{C}$, 1.5 GPa and 72 h). Olivine cubes were pre-annealed at 1400 $^{\circ}\text{C}$ and an oxygen fugacity relative to FMQ + 1 for 24 h (see text for full details). **b** Image of a double-polished hydroxylated cuboid showing the positions of laser ablation analyses



a resolution of 4 cm^{-1} . A background through air was taken at regular intervals, although the dry air purge in the sample chamber ensured consistently low atmospheric blanks. Measurements consisted of profiles across the sample using a rectangular aperture of $25 \times 100 \text{ }\mu\text{m}$, with $10 \text{ }\mu\text{m}$ steps between each measurement. Spectra were treated first with the “Atmospheric compensation” tool to remove any remaining atmospheric signal, which is part of the OPUS software suite that accompanies Bruker spectroscopic instruments. They were then baseline-corrected using the “Concave rubberband” algorithm, also part of the OPUS software, using 4 baseline points and 64 iterations. Spectra were subsequently normalised to the absorption of the silicate overtone region ($1200\text{--}2200 \text{ cm}^{-1}$) at the cuboid core to account for any variations in thickness at the rim due to polishing, before being further normalised to 1 cm using direct measurement of thickness in the wafer core using a mechanical micrometer. As a check on the correction for absorption along Ellb, one cuboid was removed from the epoxy and remounted in the orientation perpendicular to the original mount (Figure S1).

EPMA

The major element composition of olivine crystals were measured using a JEOL JXA-8200 electron microprobe at the University of Bern. An accelerating voltage of 15 kV and a current of 20 nA were used, with counting times of 20 s and 10 s on the background and peak, respectively.

LA-ICP-MS

The trace element composition of olivine crystals before and after the experimental study were determined at RSES using an Agilent 7700 quadrupole ICP-MS coupled to an in-house laser ablation setup. This setup consists of a Coherent COMPex 110 excimer laser (193 nm), which sends a pulsed laser via a series of turning mirrors and apertures to a two-volume ablation cell, upon which it is focused onto the sample surface. Ablation was conducted with a pulse rate of 5 Hz and a fluence measured just above the sample surface of between 5 and 6 mJ/cm^2 in an atmosphere of helium. The ablated material was delivered to the ICP-MS in a mixture of helium and argon, with a signal-smoother employed to homogenise the individual pulses produced in the raw signal due to the rapid wash-out times of the cell. The isotopes measured were ${}^7\text{Li}$, ${}^{23}\text{Na}$, ${}^{25}\text{Mg}$, ${}^{27}\text{Al}$, ${}^{29}\text{Si}$, ${}^{31}\text{P}$, ${}^{43}\text{Ca}$, ${}^{45}\text{Sc}$, ${}^{47}\text{Ti}$, ${}^{51}\text{V}$, ${}^{53}\text{Cr}$, ${}^{55}\text{Mn}$, ${}^{57}\text{Fe}$, ${}^{59}\text{Co}$, ${}^{60}\text{Ni}$, ${}^{61}\text{Ni}$, ${}^{63}\text{Cu}$, ${}^{65}\text{Cu}$, ${}^{89}\text{Y}$, ${}^{90}\text{Zr}$, with counting times typically around 0.01 s except for Y and Zr (0.08 and 0.15 s, respectively). Standards of NIST 610, BIR, BCR and GOR132 were measured at regular intervals between sample measurements and the laser spot size used was $81 \text{ }\mu\text{m}$ in diameter. Three spots were measured per

sample, with both the core and the rims analysed to check for compositional homogeneity. The laser data were processed using the Iolite software package, with NIST 610 used as the calibration standard and Si^{29} as the internal standard, with standard composition values from Jochum et al. (2011). Compositions of BIR, BCR and GOR132 were generally within 10% of the values reported in Jochum et al. (2005).

Results

San Carlos olivine compositions

Figure 2 summarizes the result of the initial LA-ICP-MS analyses performed to establish the compositional variability of San Carlos olivines and aid crystal selection for the experiments, whilst Table 1 shows the compositions for the six crystals selected for the experiments. The trace-element concentrations of the other San Carlos olivines are given in the Supplementary Information (SI Table A). The concentrations of the trace elements in the San Carlos olivines are very homogeneous across individual crystals and fall close to the median of the global array of upper mantle olivines, but nevertheless show a rather substantial variation with an order of magnitude range in Ti concentration and factors of 4 and 2.5 variation in Na and Cr, respectively. The forsterite contents (Mg#s) for the six selected crystals range from 89.5 to 92.0 and correlate with both Mn and Co concentrations.

FTIR spectra and substitution mechanisms

FTIR analysis of the crystals before and after the pre-anneal show no detectable water bands (Fig. 3) which, given the initial cuboid thickness of around 1.5 mm, confirms essentially anhydrous starting compositions ($< 1 \text{ ppm}$).

The polarised FTIR spectra along Ella and Ellc of the cores of the six cuboids experimentally hydroxylated at $800 \text{ }^\circ\text{C}$ and 1.5 GPa are shown in Fig. 4. The relatively minor contribution from Ellb is shown in figure S1. A number of bands are clearly identifiable within the OH-stretching region ($3650\text{--}3000 \text{ cm}^{-1}$) confirming successful hydroxylation of the starting material. By contrast, experimental hydroxylation of San Carlos olivine at the same conditions ($800 \text{ }^\circ\text{C}$, 1.5 GPa) that was not pre-annealed reveals almost no H_2O (Fig. 3), indicating that the take-up of water is enabled by the pre-anneal.

The most prominent absorption bands occur at 3612 cm^{-1} , 3572 cm^{-1} , 3525 cm^{-1} , 3353 cm^{-1} , 3328 cm^{-1} and 3220 cm^{-1} , with minor bands/shoulders at 3601 cm^{-1} , 3540 cm^{-1} , 3388 cm^{-1} and 3160 cm^{-1} . The multitude of bands is similar to those produced in the M_2 experiments of Bai and Kohlstedt (1993) in San Carlos olivine pre-annealed at high $f\text{O}_2$ (see their Figs. 2, 3), and the M_1 experiments of

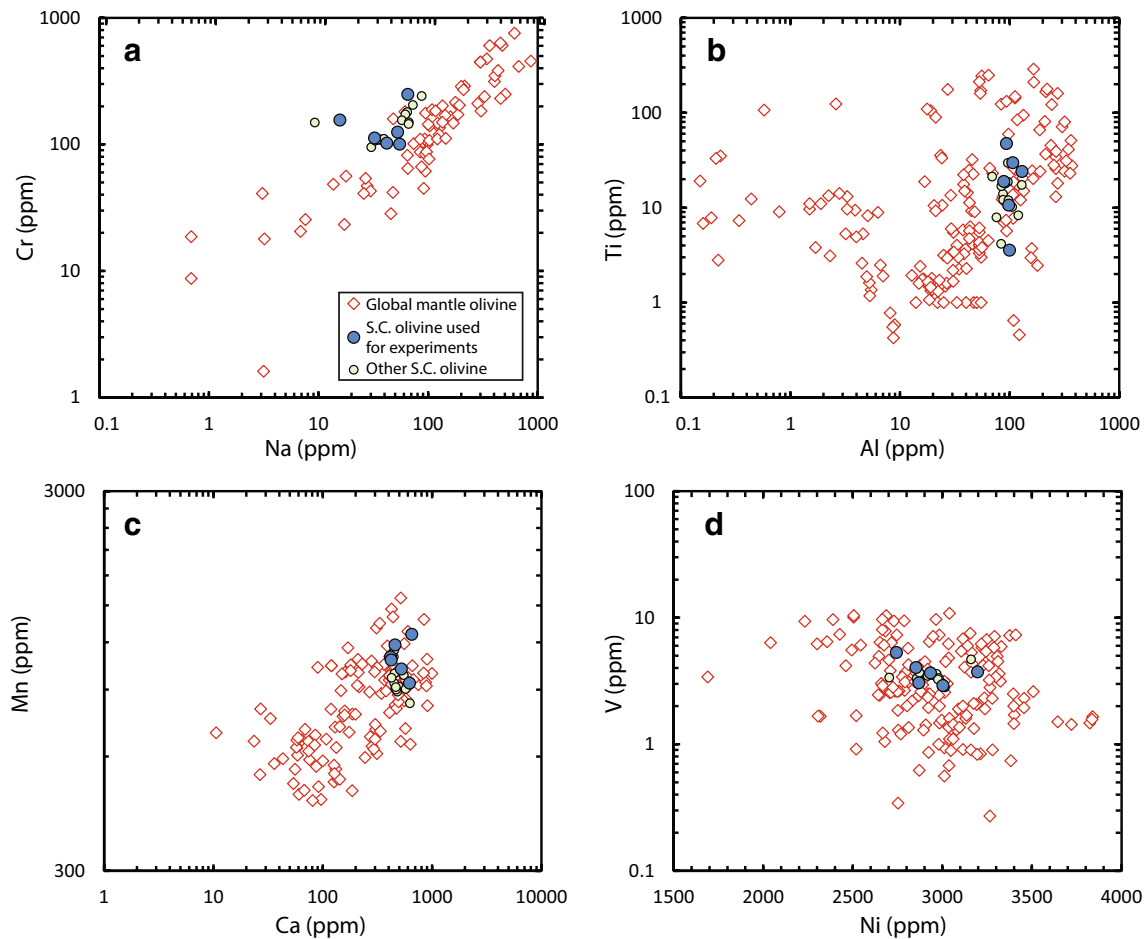


Fig. 2 Compositions of the San Carlos olivines chosen for this study, as well as additional San Carlos olivines which were not selected. For context, compositional fields for global mantle olivine are also plotted

(Neumann et al. 2004; Witt-Eickschen and O'Neill 2005; Zheng et al. 2005, 2007; Kaeser et al. 2006; De Hoog et al. 2010; Batanova et al. 2011; Ionov 2010; Pirard et al. 2013; Smith 2013)

Gaetani et al. (2014). For simplicity, absorption bands are typically grouped together, based either on their wavenumber position or their structural assignment. A commonly used terminology is “Group I” and “Group II”, referring to bands occurring between $3650\text{--}3450\text{ cm}^{-1}$ and $3450\text{--}3000\text{ cm}^{-1}$, respectively (Bai and Kohlstedt 1993; Zhao et al. 2004; Umemoto et al. 2011; Férot and Bolfan-Casanova 2012). This is somewhat useful since in many natural and experimental olivines either group I or group II bands tend to dominate over the other (Bai and Kohlstedt 1993), although this is not always the case (Fig. 4). Furthermore, bands within these respective groups respond differently to a variety of parameters, such as oxygen fugacity and composition (e.g. Bai and Kohlstedt 1993; Zhao et al. 2004). Despite this, the usage of “Group I” and “Group II” is an oversimplification of the behaviour of bands within these respective wavenumber ranges. “Group I” actually encompasses two distinct types of defect, one relating to pure Si vacancies, and the other to Ti-clinohumite point defects (Lemaire et al.

2004; Berry et al. 2005; Umemoto et al. 2011; Ingrin et al. 2013; Tollan et al. 2017a). The absorbance bands generated by these defects are very close to each other, particularly along E1a and E1b (e.g., Fig. 7 in Tollan et al. 2017a), and hence can be easily misassigned. “Group II” encompasses two further defects, one relating to the coupled substitution of a trivalent cation and a H for two Mg and one relating to two H replacing a Mg vacancy (Lemaire et al. 2004; Berry et al. 2007a; Umemoto et al. 2011; Ingrin et al. 2013; Tollan et al. 2017b). Whilst these are easily distinguished based on band shape and position, they have very different dependencies on thermodynamic and compositional variables (Tollan et al. 2015, 2017a; Blanchard et al. 2017). As a result of this, we recommend abandoning the “Group I/II” nomenclature, and instead referring to band groups based on the established point defect stoichiometries (Berry et al. 2005, 2007b; Kóvacs et al. 2010; Padrón-Navarta et al. 2014; Jollands et al. 2016; Tollan et al. 2017a):

Table 1 Trace, minor and major element data for the six San Carlos olivine crystals used in the experiments

	Crystal 1	Crystal 2	Crystal 3	Crystal 4	Crystal 5	Crystal 6
EPMA						
SiO ₂	40.79	41.44	40.79	40.73	40.81	41.06
FeO	10.06	9.92	10.87	8.42	8.54	8.46
MnO	0.14	0.14	0.16	0.15	0.13	0.10
MgO	50.02	47.50	48.31	51.08	49.73	49.95
CaO	0.07	0.06	0.13	0.08	0.09	0.12
NiO	0.35	0.38	0.40	0.41	0.36	0.43
Total	101.43	99.45	100.66	100.86	99.65	100.12
Mg#	0.899	0.895	0.888	0.915	0.912	0.913
LA-ICP-MS						
Li	1.60	1.68	1.69	1.56	1.59	2.55
Na	41.9	52.8	55.1	32.5	15.7	65.2
Al	98	94	107	88	100	130
P	31.9	45.0	38.0	25.6	25.9	33.7
Ca	418	459	651	423	524	621
Sc	3.74	4.91	5.22	4.11	4.51	3.87
Ti	10.6	47.4	29.8	18.9	3.6	24.0
V	2.91	4.03	5.30	3.05	3.66	3.72
Cr	102	125	100	112	155	248
Mn	1097	1179	1258	1076	1020	936
Co	136	146	148	132	134	140
Ni	3004	2853	2744	2869	2934	3197
Y (ppb)	20.3	30.1	33.4	19.1	5.7	30.8
Zr (ppb)	4.1	45.3	7.6	7.9	12.3	51.9

All LA-ICP-MS data are in units of wt ppm, except for Y and Zr (wt ppb) and Mg#. EPMA data are in units of wt%

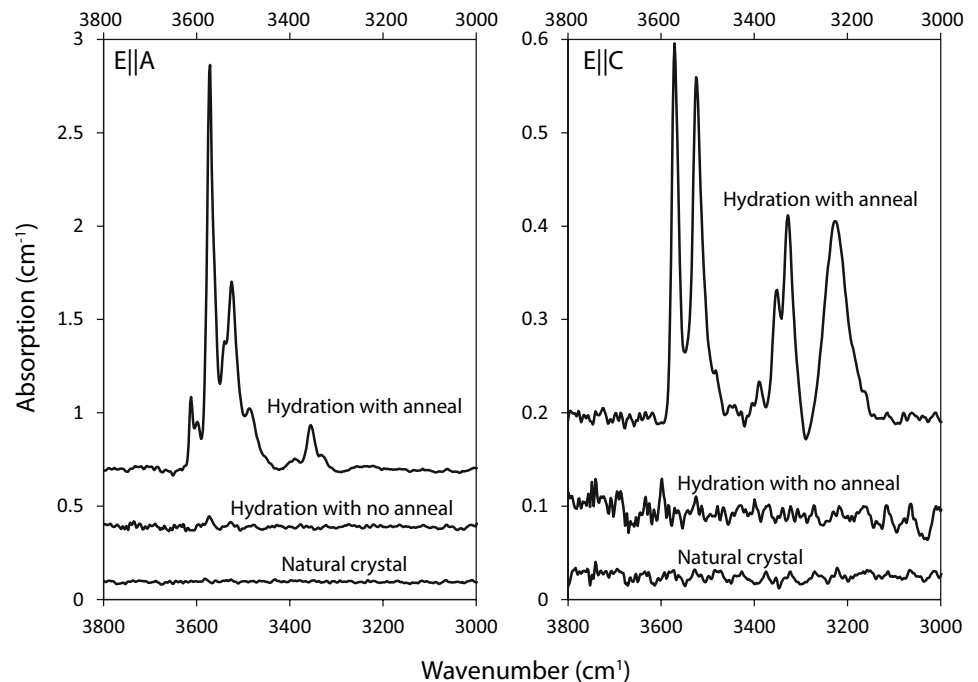
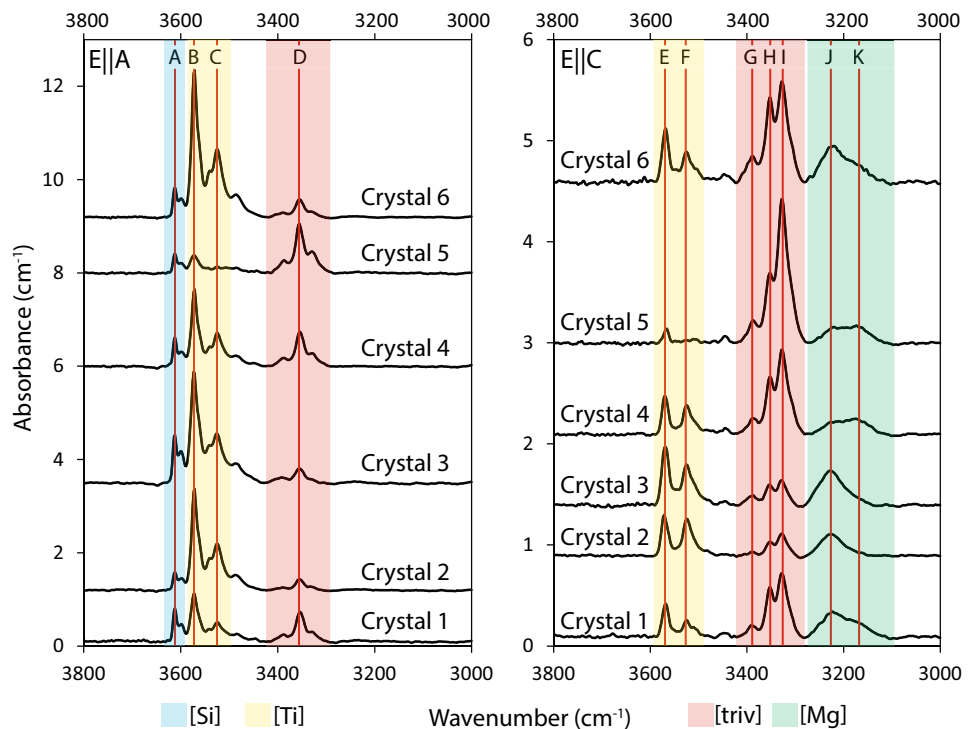
Fig. 3 FTIR spectra of San Carlos olivine cuboids before any experiment and following hydration both with and without a high temperature pre-anneal. Spectra in both E||A and E||C were measured, and are all baseline-corrected, normalised to 1 cm and offset for clarity

Fig. 4 Polarised FTIR spectra taken from the core of each crystal cube after the hydroxylation experiments. The most significant bands and the point defects they are assigned to are identified by red vertical lines and coloured shading: A = 3612 cm^{-1} ([Si]); B and E = 3572 cm^{-1} ([Ti]); C and F = 3525 cm^{-1} ([Ti]); D and H = 3353 cm^{-1} ([triv]); G = 3387 cm^{-1} ([triv]); I = 3328 cm^{-1} ([triv]); J = 3220 cm^{-1} ([Mg]); K = 3160 cm^{-1} ([Mg])



[Si]: four hydrogens charge compensating a vacant tetrahedral site (diagnostic band at 3612 cm^{-1}).

[Ti]: two hydrogens substituting onto a vacant tetrahedral site, charge compensated by Ti on an octahedral site (bands at 3572 cm^{-1} and 3525 cm^{-1}).

[triv]: one hydrogen on a vacant octahedral site charge balanced by a trivalent cation (bands between 3450 cm^{-1} and 3300 cm^{-1}).

[Mg]: two hydrogens charge compensating a vacant octahedral site (bands at 3220 cm^{-1} and 3160 cm^{-1}).

All four substitution mechanisms start with a cation vacancy in which the resulting charge deficit is compensated locally by H^+ ions bonding to O^{2-} anions surrounding the vacant cation site. In [triv] and [Mg] the vacancy is an octahedrally coordinated site and in [Si] and [Ti] the vacancy is a tetrahedral site. The four substitution mechanisms each define thermodynamic components, namely $\text{Mg}_2\text{H}_4\text{O}_4$, MgTiH_2O_4 , MgH_2SiO_4 and the various $\text{R}^{3+}\text{HSiO}_4$ components, whose chemical potentials (i.e., activities) determine the equilibrium amounts of H substituting in olivine by each mechanism, with the total H given by the sum over all four substitution mechanisms (Tollan et al. 2017a).

Whilst the [Si], [Ti], [triv] and [Mg] bands are observed in all six crystals, their intensities in both the orientations along E_{lla} and E_{llc} vary substantially from crystal to crystal (Fig. 4; Table 2). The greatest variations can be seen when comparing absorption in the [Ti] and [triv] bands. For example, crystal 3 has substantially stronger absorption at [Ti] in both orientations, whereas crystal 5 has stronger absorption

at [triv] in both orientations. Crystals 4 and 6, however, show stronger absorption at [Ti] along E_{lla}, but stronger absorption at [triv] along E_{llc}. Profiles across the cuboids reveal more-or-less homogeneous cores, but with increases in intensity of the [Si] band over a region extending approximately $200\text{ }\mu\text{m}$ from the cuboid rim (Fig. 5). Both the [triv] and [Mg] bands show subtle but more irregular variation, which often takes the form of a “W” shape, with greatest intensity at the rims and in the core and a trench of intensity in the approximate region $100\text{--}300\text{ }\mu\text{m}$ from the rim. The variations in intensity can differ markedly between crystals. The spectrum measured along E_{llb} (Figure S1) displays very little [Ti] absorbance, with no distinct peak at 3572 cm^{-1} and only a very minor shoulder at 3525 cm^{-1} . Instead, the majority of absorbance at wavenumbers above 3500 cm^{-1} is due to [Si] bands with peak centres at 3578 cm^{-1} , 3562 cm^{-1} and 3546 cm^{-1} . Bands associated with [triv] display very weak intensity, with the main peak centred at 3353 cm^{-1} . In agreement with previous work (Demouchy and Mackwell 2003; Tollan et al. 2017a), no [Mg] bands were detected in this orientation.

H₂O contents

The concentrations of H_2O in the olivines were calculated from the total absorbance, which was obtained for the individual bands by summing the normalised absorbance as measured for E_{lla} and E_{llc}, and then estimating the contribution from the b axis, which is relatively minor. This

Table 2 Absorbance and water concentrations following the hydration of cuboids cut from the six starting crystals

	Crystal 1			Crystal 2			Crystal 3			Crystal 4			Crystal 5			Crystal 6		
	Rim 1	Rim 2	Core															
Elle (Abs/cm)																		
[Si]	13.0	13.2	8.6	7.9	11.2	7.6	22.9	21.2	12.6	11.7	14.4	6.2	10.1	8.1	4.8	3.8	7.3	3.1
[Ti_3572]	17.7	15.9	13.6	54.1	63.4	48.4	35.4	34.6	30.7	21.6	24.6	20.7	6.4	5.7	4.6	28.0	26.8	23.6
[Ti_3525]	3.3	4.4	4.3	25.7	29.4	22.8	11.2	10.6	11.1	8.0	8.6	9.1	0.0	0.0	0.0	13.4	11.2	10.7
[triv]	18.0	22.5	20.5	26.3	28.2	17.3	13.1	10.9	12.5	25.2	29.0	25.6	39.4	36.2	38.9	36.6	29.5	27.3
Total	51.9	56.0	47.0	114.0	132.2	96.1	82.6	77.2	66.9	66.4	76.6	61.6	55.9	50.0	48.3	81.8	74.7	64.8
Elle (Abs/cm)																		
[Ti_3572]	6.2	5.3	4.6	10.4	10.3	10.3	12.8	12.2	8.7	8.5	7.6	5.6	4.3	3.5	1.9	6.4	6.7	4.7
[Ti_3525]	1.7	2.2	2.4	12.7	12.1	11.1	5.9	5.8	6.0	5.4	4.3	3.9	0.0	0.0	0.0	6.2	5.5	5.1
[triv]	28.6	24.0	27.8	24.3	22.3	19.7	15.5	13.6	13.3	45.9	39.0	36.6	65.5	72.8	57.6	30.3	29.4	36.3
[Mg]	19.7	23.1	20.2	31.1	28.2	25.8	22.9	27.0	21.9	16.9	18.2	12.4	11.4	21.2	12.7	7.1	10.2	7.2
Total	56.3	54.7	55.0	78.4	72.9	66.9	57.1	58.6	49.9	76.7	69.1	58.5	81.2	97.5	72.2	50.1	51.8	53.3
Total (ppm)																		
[Si]	2.4	2.5	1.6	1.5	2.1	1.4	4.3	4.0	2.4	2.2	2.7	1.2	1.9	1.5	0.9	0.7	1.4	0.6
[Ti_3572]	4.5	4.0	3.4	12.1	13.9	11.0	9.1	8.8	7.4	5.7	6.1	4.9	2.0	1.7	1.2	6.5	6.3	5.3
[Ti_3525]	0.9	1.2	1.3	7.2	7.8	6.4	3.2	3.1	3.2	2.5	2.4	2.5	0.0	0.0	0.0	3.7	3.1	3.0
Total [Ti]	5.4	5.2	4.7	19.3	21.7	17.4	12.3	11.9	10.6	8.2	8.5	7.4	2.0	1.7	1.2	10.2	9.4	8.3
[triv]	4.4	4.4	4.5	4.8	4.7	3.5	2.7	2.3	2.4	6.7	6.4	5.8	9.9	10.2	9.1	6.3	5.5	6.0
[Mg]	0.9	1.1	1.0	1.5	1.3	1.2	1.1	1.3	1.0	0.8	0.9	0.6	0.5	1.0	0.6	0.3	0.5	0.3
Total	13.2	13.2	11.8	27.0	29.8	23.5	20.3	19.4	16.4	17.8	18.4	15.0	14.3	14.5	11.8	17.5	16.8	15.2
Total*	15.0	15.0	13.4	30.8	34.0	26.8	23.2	22.1	18.7	20.3	21.0	17.1	16.3	16.5	13.4	19.9	19.2	17.3

Values are presented for *a* and *c* axes separately, and concentrations have been calculated for each of the recognised hydrous point defects, measured at the cuboid cores. Data for *a* and *c* axes are presented as absorbance units normalised to 1 cm, whilst the total concentrations have been converted to wt ppm H₂O using the following calibration factors: [Si] 0.188, [Ti] 0.188, [triv] 0.094, [Mg] 0.047. The former two values are from Bell et al. (2003), whilst the latter two are subsequently calculated based on the relationship of absorbance coefficient vs. wavenumber of Blanchard et al. (2017) Integration ranges are as follows: [Si] 3625–3590 cm⁻¹, [Ti_3572] 3590–3550 cm⁻¹, [Ti_3525] 3550–3495 cm⁻¹, [triv] 3416–3295 cm⁻¹, [Mg] 3281–3130 cm⁻¹. Total values are the sum of the *a* and *c* axes. Total* values include an additional correction for the *b* axis, which corresponds to 12% of total absorbance and 14% of the total water concentration

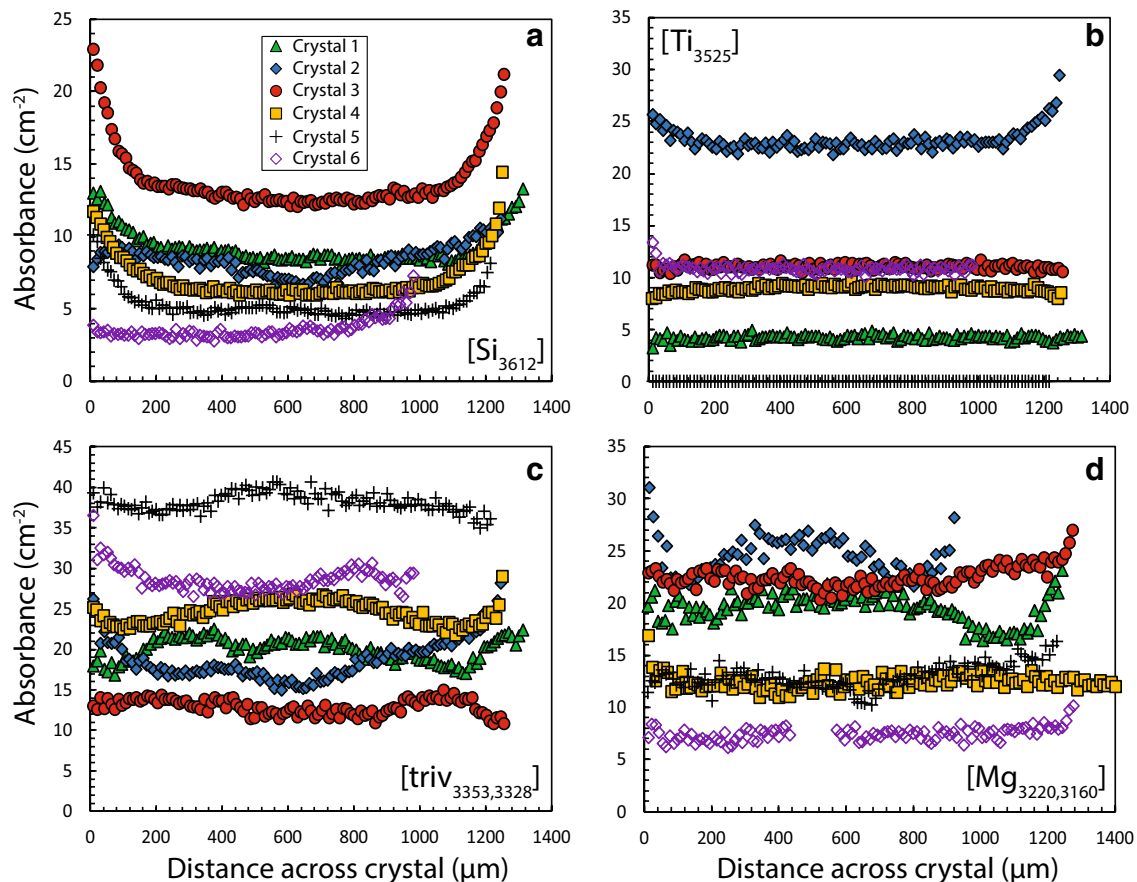


Fig. 5 FTIR profiles across hydroxylated cubes showing the integrated absorbance for bands associated with different point defects. Profiles displayed are along Ella, with the exception of [Mg] which is along Ellc. The gap in data for crystal 6 in subplot d was due to a fracture causing poor data quality. Note that only the 3525 cm^{-1} band is shown for [Ti], since the 3572 cm^{-1} has an interference from an

overlapping [Si] band (Padrón-Navarta 2014). Note that the data do not represent deconvoluted bands, merely the integrated absorbance of the measured spectra. The integration ranges for each subplot are as follows: [Si] $3625\text{--}3590\text{ cm}^{-1}$, [Ti]₃₅₂₅ $3550\text{--}3495\text{ cm}^{-1}$, [triv] $3416\text{--}3295\text{ cm}^{-1}$, [Mg] $3281\text{--}3130\text{ cm}^{-1}$. Reproducibility for a given spectrum is better than 1%

contribution was assessed in one of the cuboids to correspond to 12% of the total absorbance (Supplementary figure S1). In detail, this consists of 19% of total [Si] plus [Ti] (which could not be distinguished from each other due to the overlap of these bands, see Supplementary figure S1), 10% of total [triv] and 0% of total [Mg]. Hence, the total measured absorbance of each cuboid was further increased by these amounts (Table 2). Total absorbance was then converted to parts per million by weight (ppm) of H_2O by multiplying by a calibration factor (related inversely to the molar absorption coefficient), as indicated in the table caption. Presently, there is no consensus regarding the use of calibration factors/absorption coefficients, with a wide range of values reported in the literature (Bell et al. 2003; Kovács et al. 2010; Mosenfelder et al. 2011; Withers et al. 2012). The calibration factor of 0.188 determined by Bell et al. (2003) has been used extensively, and is consistent with values reported by Kovács et al. (2010) for the [Ti] defect and Mosenfelder et al. (2011) for bands in the wavenumber

range $3400\text{--}3700\text{ cm}^{-1}$. Furthermore, Tollan et al. (2017a) showed that using this value gives a 1:1 molar ratio of H_2O associated with the [Ti] defect to Ti concentration, as would be expected for the stoichiometry of this point defect. Hence, we use this as a reliable “anchor point” for calculating water associated from the other defect types. To do this, we utilised the study of Blanchard et al. (2017), who showed that the absorption coefficient should vary linearly with the wavenumber of infrared absorbance. Whilst the absolute values in this study are not reliable, the relative values are, indicating that the absorption coefficient for [triv] bands between 3300 and 3400 cm^{-1} should be approximately double that for the bands in the study of Bell et al. (2003). Hence, we have included a new calibration factor (0.094) which is half that of Bell et al. (2003), equivalent to an integral molar absorption coefficient of $56,900\text{ l mol}^{-1}\text{ cm}^{-2}$. Based on the same relationship, we also calculate a calibration factor for the [Mg] defect of 0.047 (integral molar absorption coefficient of $113,800\text{ l mol}^{-1}\text{ cm}^{-2}$). Withers et al. (2012)

determined an integral molar absorption coefficient of $45,200 \text{ l mol}^{-1} \text{ cm}^{-2}$ (equivalent to a calibration factor of 0.119) for olivines whose hydrous point defects, based on their infrared spectra, comprise mainly of the [Si] defect. This is in contrast to the aforementioned studies, as the high wavenumber absorbance of the [Si] bands should mean the absorption coefficient is similar to that of the [Ti] defect, or in fact slightly lower. To be consistent, therefore, we chose to use the Bell et al. (2003) value for the [Si]. However, we acknowledge that these values may be inaccurate, and hence we have also provided normalised absorbance for each defect (Table 2) in addition to our calculations of water concentration.

Using these calibration factors, the total H_2O concentrations (equivalent to a bulk measurement technique such as secondary ionisation mass spectrometry) are 13–27 ppm at the cuboid cores and 15–34 ppm at the rims. These total concentrations show no correlation with any element. However, when the absorption associated with individual bands or groups of bands are used then distinct variations appear (Fig. 6). The [Ti] bands show very strong positive correlations with Ti concentrations, in both the measured orientations (Fig. 5a). The [triv] bands show a negative correlation with Na concentration, with the exception of one data point at the highest Na concentration (Fig. 6b). This crystal has a higher Cr concentration, the significance of which will be discussed subsequently. The [triv] bands also show a negative correlation with FeO concentration (Fig. 5d), and thus a positive correlation with Mg#.

Discussion

Comparison with previous results

M-type experiments produce a metastable equilibrium, therefore, it is not expected that either the amounts of H incorporated or the substitution mechanisms by which this H is incorporated will be the same as found at global equilibrium at a given T, P, $f\text{O}_2$, $f\text{H}_2\text{O}$ and composition. Indeed, the outcomes will depend on how the M-type experiment is performed, including the initial state of the starting material. It is fallacious to suppose that a constitutive equation exists to quantify H contents in such circumstances, enabling quantitative comparison between studies. Nevertheless, there are some significant qualitative comparisons that can be made. One obvious difference between the present results and those of G-type experiments is that the latter have mostly given rather simpler FTIR spectra, indicating the dominance of one or two substitution mechanisms. For example, Matveev et al. (2001) found only [Si] substitution at low $a(\text{SiO}_2)$, and only [triv] substitution at high $a(\text{SiO}_2)$. The latter may be due to the highly oxidizing conditions

used in that study (Re- ReO_2 buffer). G-type experiments on synthetic Fe-containing compositions at high pressure ($> \sim 3$ GPa) have consistently produced olivine with only or nearly only the [Si] substitution, without significant [triv] (e.g., Smyth et al. 2006; Bali et al. 2008; Withers et al. 2011). The reason for the simpler, typically [Si]-dominated spectra is, first, the use of simple synthetic ($\text{MSH} \pm \text{F}$) systems which do not contain appreciable amounts of additional trace elements capable of generating [Ti] or [triv] absorbance, and second, the use of high pressures and water activities which favour [Si] defects over others (Padrón-Navarta and Hermann 2017; Tollan et al. 2017a). The stabilisation of [Si] at high pressure and water activity also permits significantly more water to be incorporated into olivine compared to the M-type experiments reported in this study (Kohlstedt et al. 1996; Mosenfelder et al. 2006; Smyth et al. 2006; Withers and Hirschmann 2008; Férot and Bolfan-Casanova 2012).

In contrast, M-type experiments on natural olivines often result in multiple substitution mechanisms, with four mechanisms seen in experiments on San Carlos olivine in Bai and Kohlstedt (1993), Gaetani et al. (2014) and this study. The metastable states produced in such experiments bear witness to the history of the crystal as well as to the mechanism of hydroxylation, which we now discuss.

The point-defect structure of the pre-annealed, anhydrous San Carlos olivine

Given that the main aim of the experiments is to discern how different elements in the pre-annealed San Carlos olivines affect the incorporation of H, it is important first to establish if there are any significant pre-existing correlations between elements prior to the hydroxylation experiment. To do this, we calculated the pairwise correlation coefficients between the logarithms of the mean-normalized concentrations for each pair of elements, i.e., $\text{corr}[\log(M_1)/(M^{\circ}_1), (M_2)/(M^{\circ}_2)]$. The resulting matrix of correlation coefficients is given in the Supplementary Information (SI Table B). Surprisingly, there are only a few highly significant correlations among the incompatible elements: those with values of $\text{corr}[\log(M_1)/(M^{\circ}_1), (M_2)/(M^{\circ}_2)] > 0.7$ are [Na, Y] with 0.87, [Ti, Y] with 0.77, [Ca, V] with 0.74, and [Ca, Al] with 0.72. There are two reasons why correlations between these element pairs might have been expected. First, extraction of partial melts or metasomatism would be expected to decrease or increase, respectively, all elements with similar compatibilities. This may be reflected in the correlation between Ti and Y. Second, substitution of many trace elements in olivine may require charge-balancing, which could possibly account for the correlation between Na and Y, although the lack of correlation of Li with Y or Na with Sc argues that the correlation is more likely due to the first cause, as both Na and Y are incompatible elements. Charge-balancing may also be

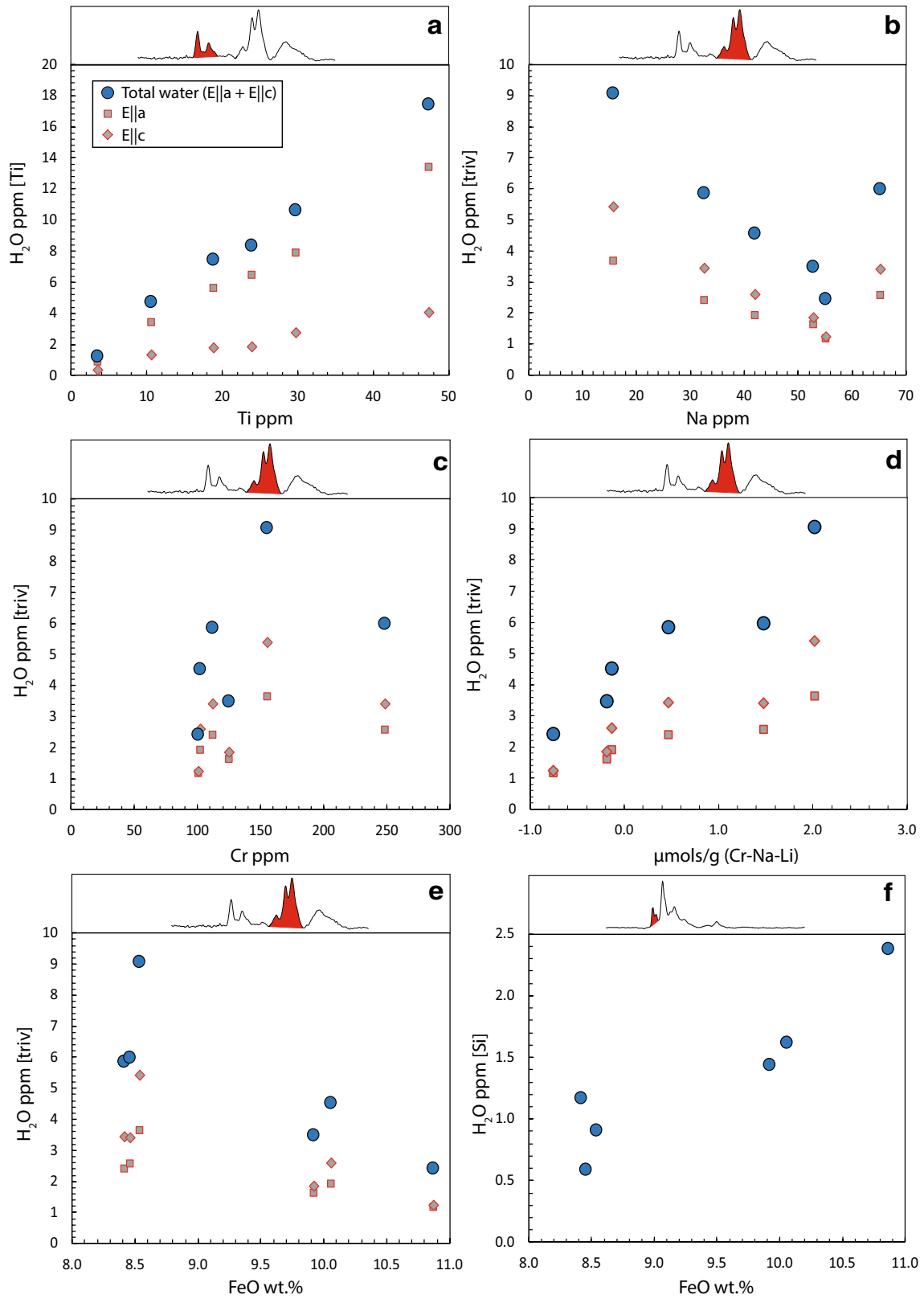
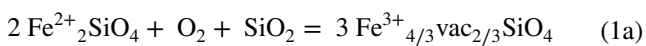


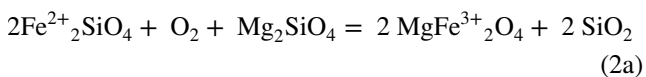
Fig. 6 Relationships between the absorbance associated with specific FTIR bands and composition. Note that in sub-figure d, units of $\mu\text{mol/g}$ are used to illustrate the competing charge balance of Na^+ , Li^+ and H^+ with Cr^{3+} . The integrated bands associated with each subplot are displayed above, and the integration ranges used stated in the caption for Table 2. Water concentrations were calculated from normalised absorbance along Ella and Elle using defect-specific absorption coefficients (see “Discussion”). Each data point was collected from the core of a different crystal. For the FTIR data, a region of approximately 200–400 μm corresponding to concentration plateaus was averaged from the profiles displayed in Fig. 5. Standard deviations are similar to or smaller than the size of the points. Note the outlier in the strong trend between Na and H_2O has 100+ ppm more Cr than the other crystals

achieved by vacancies and Fe^{3+} , neither of whose concentrations can be reliably quantified at present.

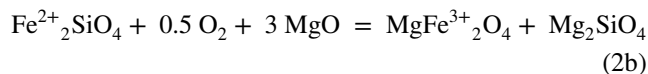
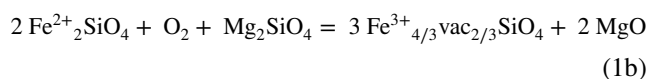
M_2 -type experiments use a two-stage process. The first stage consists of a high temperature anneal to equilibrate the point-defect structure at known conditions, followed by a low temperature hydrothermal experiment to hydroxylate this pre-set point-defect environment. Figure 3 shows the impact that the high temperature anneal (1400 °C and $\Delta\text{FMQ} + 1$) has on the defect structure of olivine, and thus the capacity for water to be incorporated during the hydrothermal anneal. The same hydroxylation condition that results in 15–34 ppm H_2O in our six pre-annealed San Carlos olivines crystals fails to produce any detectable H_2O (i.e., < 1 ppm) in unannealed San Carlos olivine crystals (M_1 experiments), demonstrating that the hydroxylation is decorating defects imposed during the pre-anneal. The higher the temperature and the higher the oxygen fugacity, the greater is the subsequent water storage capacity of olivine in M_2 experiments (Bai and Kohlstedt 1993). The most likely mechanism for this is through oxidation of Fe^{2+} and Cr^{2+} to Fe^{3+} and Cr^{3+} , either charge-balanced by associated metal vacancies ($\text{R}^{3+}\text{vac}_{4/3}\text{SiO}_4$) or by a coupled octahedral-tetrahedral site mechanism ($\text{MgR}^{3+}_2\text{O}_4$). Note that the following equations are written such as to maintain the same basic olivine unit cell stoichiometry (SiO_4) in each reaction, although at present there are no thermodynamic data for these end-member components. For the first mechanism, the reaction is:



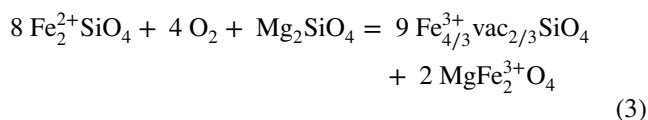
and similarly for Cr^{2+} oxidizing to Cr^{3+} . For the second mechanism, the reaction is:



Here as elsewhere in this paper we have written the reactions in terms of SiO_2 as the necessary oxide component for simplicity, but the same reactions may also be written with MgO :



The latter formulation (1b) and (2b) make clear that reactions (1a) and (2a) do not imply diffusion of SiO_2 to maintain stoichiometry and charge balance, and these would more likely be maintained by diffusion of divalent cations, that is, a combination of Mg^{2+} and Fe^{2+} in natural olivines like the San Carlos olivines used in this study. Reaction (1) consumes SiO_2 and is favoured by high $a(\text{SiO}_2)$, as imposed by buffering by pyroxene, whereas reaction (2) produces SiO_2 , and would, therefore, be favoured by buffering by magnesiowüstite. In the first mechanism, two moles of olivine are oxidized to three moles with the creation of octahedral site vacancies, while in the second mechanism, one mole of olivine reacts to two moles without vacancy formation. A possibility is that both mechanisms proceed coupled to each other for kinetic reasons, as indicated by summing (1b) and (2b) to eliminate MgO , which gives:



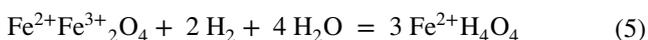
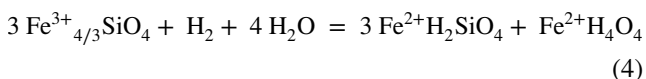
This reaction can progress into the crystal with only the diffusion of M-site cation vacancies required, producing a metastable state in which 75% of the Fe^{3+} is in the vacancy-coupled component and the 25% in the octahedral-tetrahedral coupled component.

At the temperature of the pre-anneal used here (1400 °C) diffusion of octahedral vacancies is several orders of magnitude faster than cation diffusion (Kohlstedt and Mackwell 1998). Vacancy diffusion has been proposed to account for the rapid relaxation times of electrical conductivity after step changes in oxygen fugacity from 1100 to 1300 °C (Wanamaker 1994), and may also account for the rapid redox equilibration of olivine-hosted melt inclusions with oxygen fugacity externally imposed by gas-mixing at 1250 °C (Gaetani et al. 2012). Based on the rates determined in these studies, the oxidation reaction (4) should equilibrate over the volume of the cuboids used in this study, without any significant change to the other aspects of chemical composition, including the concentrations of minor and trace elements such as Na, Al, Ti and Cr, whose diffusivities as measured in chemical diffusion experiments are orders-of-magnitude slower (Spandler and O'Neill 2010). Indeed, core and rim LA-ICPMS measurements of the crystals show no compositional zoning, both in the natural crystals and also the cuboids following hydroxylation.

Hydroxylation mechanisms of the pre-annealed San Carlos olivine

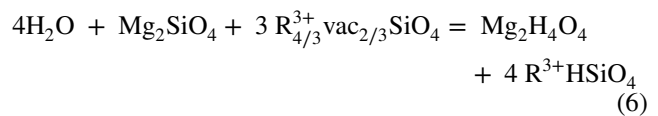
How hydrogen is incorporated into olivine crystals during the hydrothermal anneal in M-type experiments requires consideration of the metastable equilibrium state towards which the crystal progresses, as well as the kinetics of this progress. These kinetics, like most chemical kinetics, are thermally activated, following an Arrhenius relationship (e.g., Padron-Navarta et al. 2014 and references therein). Some crystals show patterns of zoning in H contents after hydroxylation that bear witness to more than one mechanism in a given experiment, distinguished by different kinetics (Kohlstedt and Mackwell 1998; Jollands et al. 2016). Here, it is necessary to differentiate between those M-type experiments in which the hydroxylation is performed at high enough temperatures to change significant aspects of the point-defect structure of the crystal other than its H content, and M-type experiments in which this other point-defect structure does not change. While it is probable that most M-type experiments fall in between these ideals, the experiments of both Grant et al. (2007b) and Gaetani et al. (2014), at temperatures of 1100 and 1200 °C, respectively, showed that the H concentrations in their olivines depended on the fO_2 during the hydroxylation stage. In addition, in the latter study, similar H contents were achieved whether the olivine was pre-annealed or not. By contrast, the experiments of Bai and Kohlstedt (1993), mostly at 1000 °C for 4 h, preserved the different fO_2 and $a(SiO_2)$ imposed during the pre-anneal. All these studies were on San Carlos olivine. The hydroxylation stage of this study, also on San Carlos olivine, was at a temperature sufficiently low (800 °C) that the point-defect structure of the olivines should likewise be largely preserved from their pre-anneal.

For each hydroxylation mechanism in an M-type experiment, there are two interconnected aspects, the reaction by which H is incorporated into olivine at the crystal interface, and the subsequent mechanism by which this H then diffuses through the crystal to produce the substitution mechanism(s) imaged by infra-red spectroscopy. Both aspects require that charge balance is maintained. One possibility termed “proton-polaron”, first postulated by Mackwell and Kohlstedt (1990), involves incorporation of H via reduction of Fe^{3+} followed subsequently by rapid interstitial diffusion to decorate other pre-existing point defects. Combined with the equations presented above for the pre-anneal point defect composition, this mechanism can be expressed by the following equations:



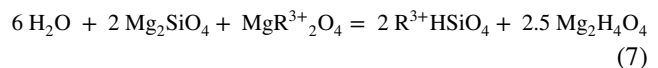
For either (4) or (5), the reaction at the surface of the olivine crystal uses the O available from the H_2O to produce the hydroxylated olivine components on the right-hand side of the equations and is dependent on fH_2 . The H and its associated vacancies in these components can then move through the lattice without the movement of other species. Reaction (4) produces mostly the [Mg] substitution with a lesser fraction of [Si], in the ratio 3 to 1, whereas reaction (5) produces all [Si]. The close association of the infra-red O–H stretching frequencies with the identity of the R^{3+} cation in the [triv] mechanism found experimentally by Berry et al. (2007a) is one item among many that shows that charge-balance among point-defects in olivine is achieved on the unit-cell scale (e.g., Balan et al. 2011; Blanchard et al. 2017). Therefore, adding H^+ requires removing a cation (one Mg or Fe^{2+} for two H^+) or reducing Fe^{3+} or Cr^{3+} to Fe^{2+} or Cr^{2+} . Only the latter charge-balancing mechanism avoids a cation flux, making it potentially fast.

Whilst the proton-polaron mechanism is viable and has gained significant traction since it was first postulated, the implied dependence on fH_2 has not yet been documented. Instead, other mechanisms that also require only the movement of protons and vacancies through the olivine crystal lattice are possible, which do not depend on fH_2 during hydroxylation. One such reaction, which also depends on the oxidation of some Fe^{2+} to Fe^{3+} during the pre-anneal, and also only requires a flux of H and vacancies, is:



There seems no reason to suppose that this reaction and the subsequent diffusion of H and vacancies would be any slower than the “proton-polaron” mechanism. In this reaction, H substitutes in two components, [Si] as well as [triv], with the substituting H in the ratio 1:1. Reaction (6) produces hydroxylated Si vacancies, but is independent of $a(SiO_2)$, explaining why a substitution mechanism favoured by low $a(SiO_2)$ may appear as an important mechanism at high $a(SiO_2)$ in the metastable thermodynamic state of an M_2 type experiment.

The analogous reaction for the hydroxylation of the $MgR^{3+}_2O_4$ component, in which an octahedral R^{3+} cation is charge-balanced by another R^{3+} cation replacing Si in the tetrahedral sites (e.g., $MgFe^{3+}_2O_4$, $MgCrAlO_4$, etc.) is:



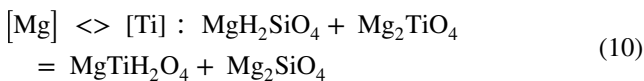
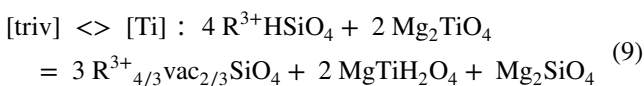
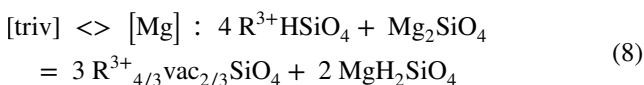
which produces H substituting mainly by [Si]; the ratio of H in [Si] to that in [triv] is 5:1.

Both these two hydroxylation mechanisms require R^{3+} cations. In the case of Fe and Cr, both of which can exist in either a 3+ or 2+ oxidation state, this requires that the

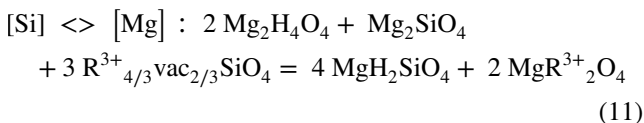
precursor olivine was crystallized or pre-annealed at relatively oxidising fO_2 conditions, as demonstrated by Bai and Kohlstedt (1993). This observation shows that other hypothetical reactions that would also allow the rapid substitution of H without R^{3+} cations do not happen, at least in the timescales of existing experimental studies.

Exchange equilibria between the four different substitution mechanisms

Whatever the mechanism(s) by which H is incorporated initially, it may then redistribute to the other substitution mechanisms, which may be anticipated to proceed rapidly because the distances involved are on the length scale of a few unit cells only. These exchange equilibria are essentially analogous to order–disorder equilibria between crystallographically distinct sites. Three of these mechanisms are isochemical:



Formation of [Si] by redistribution of H is given by



and is notable in not being isochemical, instead requiring the presence of an additional $\text{MgR}^{3+}_2\text{O}_4$ component. Quantifying these redistribution reactions requires knowledge of the activities of all hydrous point defects, total H concentration and not only the concentrations of all R^{3+} cations (including Fe^{3+}) but also their speciation among the possible components. This is currently beyond our capabilities, however, the qualitative understanding of these potential mechanisms of redistributing H between available defect sites is essential to interpreting the present results and previous experimental work. In summary, it is to be expected that the metastable state produced by hydroxylation of olivine in an M-type experiment could differ considerably in both the amount of H and its substitution mechanisms from that found in the state of global equilibrium attained in a G-type experiment at the same T, P, fO_2 , fH_2O and olivine composition. The goal of the two-stage “M₂” type of experiment used in this study aims in its simplest form for the pre-anneal to be

sufficiently long to achieve equilibrium of the point-defect structure of the crystal under the pre-annealing conditions, while the hydroxylation stage should be long enough to diffuse H into the crystal to decorate these point defects, but not too long to reset them.

The different hydroxylation reaction mechanisms separated by diffusion

Whilst the mechanisms above explain the rapid hydroxylation mechanism responsible for near-homogeneous levels of H_2O in the cores, the enhanced amounts of H in the rims of the crystals imply a second reaction mechanism with slower diffusion rates. We modelled the diffusion profiles exhibited by the [Si] point defect using the diffusion equation for symmetrical, concentration-independent diffusion into a finite slab from an infinite source:

$$C_X = (C_{\text{rim}} - C_{\text{core}}) \left[0.5 * \operatorname{erfc} \frac{x}{2\sqrt{Dt}} + 0.5 * \operatorname{erfc} \frac{X-x}{2\sqrt{Dt}} \right] + C_{\text{core}} \quad (12)$$

where C_X is the concentration at distance x from the interface, C_{rim} and C_{core} are the concentrations at the rim and core, respectively, X is the total width of the diffusion profile, D is the diffusivity ($\text{m}^2 \text{s}^{-1}$) and t is the duration of diffusion in seconds. Applying this to the measured concentration gradients for crystal 3 produces values of $\log_{10}D$ of -13.9 ± 0.2 for diffusion along Ella for [Si] (Fig. 7). The “W” shaped profiles can be modelled by diffusion of H associated with a particular substitution mechanism ([triv] or [Mg]) out of the crystal, which may be explained by annihilation of the enabling point-defect environment (Padron-Navarta et al. 2014). The required diffusion rates are intermediate between the fast mechanism responsible for the homogeneous cores, and the slower mechanism responsible for the increasing H at the edges.

The calculated diffusion rate for the [Si] bands is indistinguishable from Jollands et al. (2016) for Ti-doped forsterite starting materials. Hence, we similarly interpret this second mechanism of hydrogen incorporation and diffusion to be via associated vacant octahedral sites. An important distinction must thus be made between the diffusion of hydrogen and the site that it occupies at any given point within the lattice. This is most obvious in the case of [Si] distribution, since the diffusion of the defect itself is extremely slow (Padrón-Navarta et al. 2014) relative to the Mg vacancy mechanism. The simple explanation is thus that hydrogen diffuses along Mg vacancies before making a hop on the scale of interatomic distances to decorate an adjacent Si vacancy. To what extent this slower diffusion mechanism is influenced by the buffering environment of the hydroxylation is unclear from these experiments alone, since this experimental stage

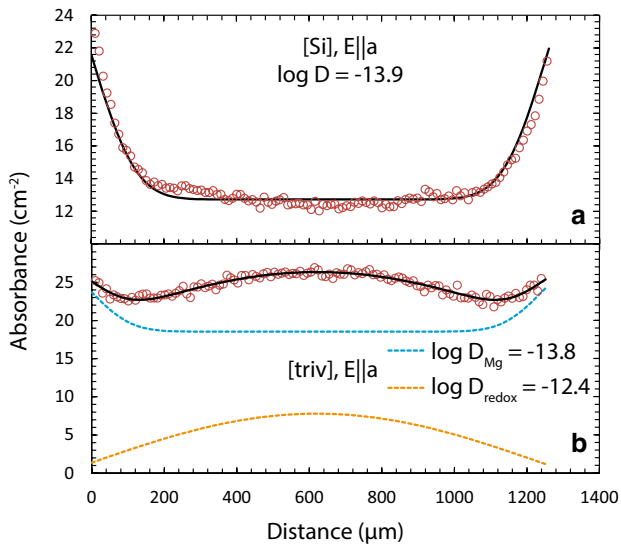


Fig. 7 Diffusion modelling of profiles for different point defects from crystal 3 (**a**) and crystal 4 (**b**). The methodology and equation used are described in the text. Note for the [triv] profile, two different mechanisms (D_{Mg} and D_{redox}) were modelled and summed to give a “bulk” diffusion profile

was conducted under a single set of conditions. It remains to explain the curious W-shaped profiles seen in the concentrations of the [Mg] and [triv] substitutions in some of the crystals (Figs. 5, 7). Although the shape of these profiles can be described algebraically with a third diffusion mechanism (Fig. 7), such diffusion would imply a fraction of H_2O escaping from the crystal against the gradient of $f\text{H}_2\text{O}$, which seems unlikely. We, therefore, suggest that this effect is not a separate diffusion mechanism, but a consequence of the redistribution of the H-containing components in response to the change in total H concentration along the diffusion gradient of the slow diffusion mechanism. Whilst it is difficult to describe these exact relationships given the restrictions imposed by the current dataset, it is likely that they will be sensitive to the specific composition of each crystal, which would explain why the W-shaped profiles are more apparent in some crystals than others (Fig. 5).

The role of titanium

The Ti concentrations in the six San Carlos olivine crystals used in this study span an order of magnitude, whilst still falling comfortably within the range of typical upper mantle olivine (De Hoog et al. 2010; Fig. 2), making them ideal for this experimental study. Following hydroxylation, there is an almost perfect correlation between Ti concentrations and the absorption of the [Ti] bands at 3572 and 3525 cm^{-1} (Fig. 6) in the cores of the crystals. These bands have been identified as being due to the Ti-clinohumite

point defect by experimental studies comparing olivines doped with Ti with those not so doped (Berry et al. 2005; Kóvacs et al. 2010; Padrón-Navarta et al. 2014; Faul et al. 2016; Jollands et al. 2016; Tollan et al. 2017a; Padrón-Navarta and Hermann 2017). On the other hand, Gaetani et al. (2014) stated that their experimental data “argue strongly against a Ti-clinohumite-like defect being the most important mechanism for incorporation of H into Ol in the shallow upper mantle”, partly on the grounds that there was no statistical correlation between the concentrations of total H and Ti in their experiments. Although this conclusion seems to indicate that the experimental results of Gaetani et al. (2014) are in conflict with those of this study, they are not. Gaetani et al. (2014) examined only four of their samples by FTIR, but these few spectra are sufficient to show, as in this study, that their olivine crystals contained H in all of the four expected substitution mechanisms, [Si], [Ti], [triv] and [Mg] (see their Figs. 11 and 12). Therefore, as for this study, no simple correlation between total H (that is, H summed over all four substitution mechanisms) and Ti concentrations is expected. Furthermore, since the majority of measurements were done by secondary ionisation mass spectrometry (a bulk rather than defect-specific measurement technique) it is completely consistent that the total water contents exceed that predicted from Ti alone, since other substitution mechanisms are clearly contributing to this bulk water content. To show the association with Ti concentration (Fig. 5), it is necessary to deconvolute the spectra into the contributions from each of the four main absorption mechanisms. Gaetani et al. (2014) instead divided their spectra according to the broad spectral ranges of the old “Group I” and “Group II” classification. The absorbances for “Group I” bands, therefore, combine the contributions from both the [Si] (3612 cm^{-1}) and the [Ti] mechanisms (3572 and 3525 cm^{-1}). Allowing for this, the correlation between Ti and the H associated with [Ti] appears reasonable for their three samples hydroxylated at high $a\text{H}_2\text{O}$. The fourth sample, hydroxylated in $\text{H}_2\text{O}-\text{CO}_2$ fluid with $X_{\text{H}_2\text{O}} = 0.185$, has lower H, which is as expected from the previous experimental work examining the variation of H incorporation by [Ti] at $a\text{H}_2\text{O} < 1$ (Tollan et al. 2017a).

The results of this study reaffirm the great stability of the [Ti] substitution in incorporating H in olivine relative to other substitutional mechanisms, as predicted by Walker et al. (2007). The consequence is that in many upper-mantle olivines, the [Ti] mechanism is the main substitution mechanism for the observed H (e.g. Demouchy et al. 2006; Peslier and Luhr 2006; Grant et al. 2007a; Schmädicke et al. 2013; Denis et al. 2013), and often the only mechanism discernible by infra-red spectroscopy, despite the low concentrations of Ti in such olivines (Fig. 2b). What remains unclear at this point is

the relative stability of the [Ti] defect compared with others at the higher pressures of the asthenospheric mantle, particular the [Si] defect which dominates in higher pressure (> 3 GPa) experiments (Smyth et al. 2006; Withers and Hirschmann 2008; Padrón-Navarta and Hermann 2017), although, as Qin et al. (2018) show, the [Mg] defect could become increasingly significant at higher temperatures. One difficulty with this is that many high pressure G-type experiments have neglected Ti as part of the starting composition. Three exceptions to this are Withers and Hirschmann (2008), who had a separate Ti-bearing composition in addition to Ti-free compositions, Mosenfelder et al. (2006) who used natural Ti-bearing olivines and Padrón-Navarta and Hermann (2017) who used natural olivine-bearing starting material. Withers and Hirschmann (2008) performed G-type experiments at 8 GPa and found no evidence for increased water solubility in olivine, nor could they identify the typical [Ti] bands in their FTIR spectra, which are instead dominated by [Si] absorbance. Mosenfelder et al. (2006) show infrared spectra for olivines equilibrated experimentally at 5.65–12 GPa which likewise show no evidence for the [Ti] mechanism. Padrón-Navarta and Hermann (2017) performed a series of experiments from 0.5 to 6.0 GPa, and in contrast found [Ti] bands at all pressures, although from approximately 3.0 GPa [Si] bands increase significantly and eventually dominate. These studies thus clearly indicate that at pressures greater than approximately 3.0 GPa in the mantle, the contribution from [Si] to total water content increases significantly (even under orthopyroxene-buffered conditions). One significant point of these studies, however, is that they were conducted under relatively high water activities, that may only prevail in the mantle under very specific conditions, such fluid-release from subducted slabs (Padrón-Navarta and Hermann 2017). At the much lower water activities of fluid-free sub-solidus mantle it is possible that [Ti] defects play a more significant role, even at high pressure (Tollan et al. 2017a). Experiments investigating these specific conditions will be important to establish the veracity of this.

The role of trivalent cations

The experimental study of Berry et al. (2007a) showed that doping forsterite with a variety of trivalent cations produced absorption bands in the wavenumber region 3450–3300 cm^{-1} . Furthermore, they showed that the wavenumber of the most intense band correlated with the ionic radius of the trivalent cation used in the experiment, theoretically permitting identification of the charge-balancing trivalent species when such bands occur in natural olivine. In practice this has proved difficult, because the nature of

the bands produced by Berry et al. (2007a) do not reproduce precisely the exact band shapes and positions observed in natural systems. This is most likely due to the presence of substantial Fe^{2+} and minor amounts of other components in natural olivines, which change the geometries of the octahedral sites, resulting in band shifts and band broadening (Blanchard et al. 2017). Furthermore, in natural olivines only three trivalent cations (Al, Fe and Cr) are typically present in sufficient concentrations such that they could plausibly be responsible for generating the measured [triv] absorbance (De Hoog et al. 2010), which explains the lack of significant variation in the positions of the most intense [triv] bands when inspecting published natural spectra. However, the bands produced by Al, Fe and Cr still have sufficiently different absorption characteristics that it becomes possible in some situations to distinguish between their relative contributions in natural systems, as demonstrated by Tollan et al. (2015) who found that a combination of Cr and Fe are most likely responsible for [triv] bands in upper mantle olivine.

In contrast to these previous studies, our hydroxylation experiments show limited correlation with the concentrations of any trivalent species (Fig. 6). It should be pointed out that this cannot be due to inter-crystal variations in $\text{Cr}^{2+}/\text{Cr}^{3+}$ and $\text{Fe}^{2+}/\text{Fe}^{3+}$ ratios, since all crystals were annealed and hydroxylated under identical redox conditions. Instead, the strongest correlation is a negative one with a monovalent species, Na^+ (Fig. 6b), which illustrates a previously unrecognised complication. The lower [triv] absorption observed at higher Na concentrations can be explained if Na, which occupies octahedral sites, charge balances Cr^{3+} and Fe^{3+} as the substitutions $\text{NaCr}^{3+}\text{SiO}_4$ and $\text{NaFe}^{3+}\text{SiO}_4$. The Cr^{3+} and Fe^{3+} tied up in these substitutions as opposed to the vacancy-coupled substitutions $\text{Cr}^{3+}_{4/3}\text{SiO}_4$ and $\text{Fe}^{3+}_{4/3}\text{SiO}_4$ are not available to bond with H diffusing into the olivine structure. The primary significance of Cr^{3+} and Na^+ can be seen by plotting the difference in their molar concentrations against $\text{H}_2\text{O}^{[\text{triv}]}$, which generates a strong positive relationship (Fig. 6d), with the negative intercept expected from the presence of Fe^{3+} , some of which will also be charge-balanced by Na. We also note that not all the measured Cr will be in the 3+ oxidation state (Jollands et al. 2018). It is probable that Li plays a similar role, however, its molar abundances is subordinate to those of Na (from 9 to 25% in our six crystals).

The concentrations of Fe^{3+} in the pre-annealed crystals are not known, however, reactions (1)–(3) show that they increase proportionally to the Fe_2SiO_4 component of the olivine. The range of $\text{FeO}^{\text{total}}$ concentrations in the six olivines of this study is rather limited (8.4–10.9 wt.%), hence the range of Fe^{3+} concentrations should be modest: specifically, the relative standard deviation of the Fe content is less than a third of that of the Cr content. Despite the obvious expectation that [triv] absorbance should correlate with Fe^{3+} , as

emphasised in previous studies (Berry et al. 2007a; Grant et al. 2007b; Tollan et al. 2015; Blanchard et al. 2017), we observe a small negative trend (Fig. 6e) rather than the positive trend that may be anticipated. With the multitude of substitution mechanisms as discussed above, this may just be coincidence.

Given these complexities, our six crystals do not show a wide enough range in Al contents to identify any effect of this component. Aluminium was one of the trivalent elements contributing to the [triv] substitution identified by Berry et al. (2007a), with characteristic bands at 3350, 3344 and 3322 cm^{-1} , which are potentially obscured by the [triv] bands associated with Fe^{3+} and Cr^{3+} in natural-composition olivines. However, [triv-Al] was shown by Grant et al. (2007a) to be the major mechanism of H incorporation in Fe-free forsterite crystallized from melts in the system $\text{Mg}_2\text{SiO}_4\text{-NaAlSi}_3\text{O}_8\text{-H}_2\text{O}$ at 1.0–2.5 GPa (G-type experiments). It has also been suggested to be a quantitatively significant enabler of H incorporation in olivine (Hauri et al. 2006; Férot and Bolfan-Casanova 2012), but only from empirical correlations of total H against Al contents. The results of this study show that such correlations are at best only indicative, given the manifold complexity of H substitution in multicomponent olivines. In a case where compositional variables could be better constrained, Tollan et al. (2015) showed that Al was not correlated with the H concentration profiles in the olivine porphyroclast of their xenolith, in which the separate contributions of Cr^{3+} and Fe^{3+} could be clearly resolved.

There are reasons to suspect why Al in olivine may not significantly enhance H incorporation in natural-composition olivines. Although a small proportion of Al in olivine substitutes by the octahedral site vacancy mechanism as $\text{Al}_{4/3}\text{SiO}_4$ (Zhukova et al. 2017), most Al substitutes by the octahedral-tetrahedral charge balance mechanisms (MgAl_2O_4 , $\text{MgCr}^{3+}\text{AlO}_4$, etc.) with short range order between the octahedral and tetrahedral R^{3+} cations (Evans et al. 2008). Hydroxylation of R^{3+} cations substituting by this mechanism produces [Si] to [triv] in the ratio 5 to 1 (reaction 7), which is not observed, suggesting that the free energy of reaction (7) is unfavourable, and the presence of Al could actually reduce the amount of Cr^{3+} and Fe^{3+} available for hydroxylation by reaction (6). Therefore, a positive Al correlation between Al and H in olivine would not be expected in natural environments where there are alternative substituting mechanisms available. By this argument, Al could actually reduce the amount of Cr^{3+} and Fe^{3+} available for hydroxylation by reaction (6). Thus, Al will not be influential in natural environments where there are alternative substituting mechanisms available.

Hauri et al. (2006) deduced from an empirical correlation between Al and the partition coefficient of H between olivine and silicate melt in olivine/melt partitioning experiments

(i.e., G-type experiments) that the H substitution in olivine may be associated with Al. The H was analysed by SIMS, and is the total H from all the substitution mechanisms. FTIR fingerprinting of the substitution mechanism in such experiments is not feasible at present. In apparent contradiction to these results, Gaetani et al. (2014) found a negative correlation between total H and Al in olivine. They explained this as being due to Al decreasing with increasing aSiO_2 , but this is implausible. The Al concentrations in the olivines of these experiments are within the range of typical San Carlos crystals from the Cr-diopside suite, giving no reason to suppose that they were not the original concentrations, and not a reflection of aSiO_2 . San Carlos olivines from the Cr-diopside suite are thought to come from an essentially uniform chemical environment as regards aSiO_2 , namely saturation with orthopyroxene.

The [Si] and [Mg] substitution mechanisms

The OH stretching bands at high wavenumbers ($> 3500 \text{ cm}^{-1}$) in olivines are potentially from at least three substitution mechanisms, namely [Si], [Ti] and, where boron is present, the [B] substitution mechanisms (Ingrin et al. 2014). The [Si] substitution is the dominant one in many experiments, particularly at high pressure, where the $\text{a}(\text{H}_2\text{O})$ is high and/or where aSiO_2 is low (Tollan et al. 2017a), producing olivines with a complex array of bands, including strong absorbance bands in both the Ellb and Ellc directions (Matveev et al. 2001; Mosenfelder et al. 2006; Withers and Hirschmann 2008; Withers et al. 2011; Tollan et al. 2017b; Padrón-Navarta and Hermann 2017). These [Si] bands rarely contribute significantly to the total water content of natural olivines from upper mantle or basaltic phenocrysts, however, bands centred at 3612 cm^{-1} , 3600 cm^{-1} , 3580 cm^{-1} and 3566 cm^{-1} are frequently found as minor features (Figs. 3, 4, supplementary figure). In olivines equilibrated at higher pressures, for example those from kimberlite-hosted xenoliths, [Si] bands can occasionally dominate (e.g., Matsyuk and Laner 2004). In this study, only the 3612 cm^{-1} can be clearly distinguished from bands related to other defects, and despite the small range of concentrations, there is a distinct positive correlation with FeO. This is best explained through the stabilisation of the pure hydrated Si defect, which as Blanchard et al. (2017) showed, involves Fe^{2+} as a nearest neighbour, occupying an M1 site.

Bands related to Mg vacancies are strongly polarised along Ellc in agreement with previous experimental results (Demouchy and Mackwell 2003; Lemaire et al. 2004) and theoretical calculations (Walker et al. 2007). They are distinguished through a much broader shape, causing some difficulty in defining the peak centroids precisely. The [Mg] absorption can typically be separated

into two overlapping bands, one centred at approximately 3160 cm^{-1} and one at approximately 3220 cm^{-1} , with the intensity of these bands varying considerably. Both natural and experimental olivines can display either or both of these bands at varying proportions, which some previous studies suggested relates to hydration of M1 and M2 site vacancies (e.g., Lemaire et al. 2004). Blanchard et al. (2017) however concluded that only the M1 site is hydrated causing a single band centred at 3160 cm^{-1} in pure forsterite, and that generation of the 3220 cm^{-1} is instead due to Fe sharing a corner or edge with a hydrated M1 site. The olivines in this study display varying proportions of the two [Mg] bands (Fig. 4), and whilst the total absorption does not correlate with any other element, the ratio of these two bands shows a distinct correlation with Mg#, such that the band at 3220 cm^{-1} is more intense at lower Mg#s (Fig. 8), in qualitative agreement with the theoretical calculations of Blanchard et al. (2017).

Compositional controls on water storage capacity of the upper mantle

Our experiments cover olivine compositions typical of the uppermost mantle and, therefore, provide a constraint on how naturally varying concentrations of trace elements may impact the water storage capacity of olivine. Experiments on two-phase olivine-fluid systems have provided most of our information on H in olivine, but may be a misleading guide to olivine storage in the mantle if it is overlooked that T-fH₂O conditions in the mantle are limited compared to those accessible in the two-phase experiments by partial melting at higher temperatures, or by buffering with

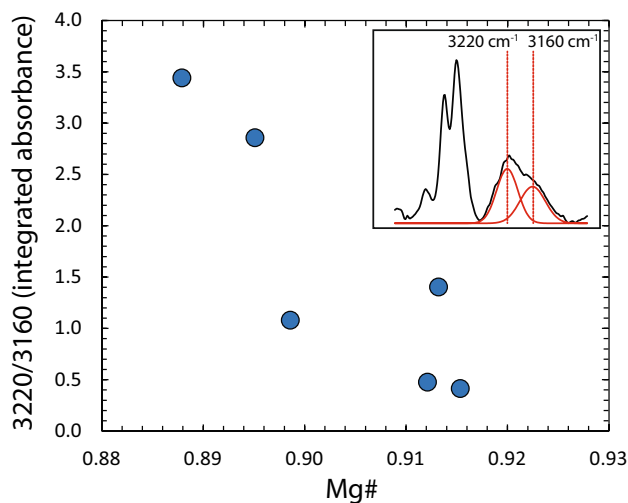


Fig. 8 Relationship between the integrated absorbance ratio of deconvoluted bands that comprise the [Mg] defect and Mg#. Deconvoluted bands were calculated using a multiple linear least squares regression and Gaussian band profile

amphibole and/or phlogopite at lower temperatures (e.g. Niida and Green 1999; Kovács et al. 2012; Green et al. 2014). Hence, we propose that at less than about 3 GPa and in the presence of the usual additional phases in upper mantle peridotite, namely orthopyroxene, clinopyroxene and an aluminous phase, and perhaps amphibole and/or phlogopite, trace element-related defects are the most important mechanism for incorporating water in olivine. The role of both [Si] and [Mg] defects are minimal, as demonstrated through our experimental study and analyses of natural samples (Demouchy et al. 2006; Peslier et al. 2008; Soustelle et al. 2010; Denis et al. 2013). This is not to say that, at pressures higher than approximately 3 GPa, [Si] defects become increasingly significant, particularly at the high water activities that two-phase olivine-fluid experiments can access (Tollan et al. 2017a; Padrón-Navarta and Hermann 2017). However, even at these conditions trace element-related defects may remain significant if the concentrations of the trace elements themselves are high enough (Peslier et al. 2010; Padrón-Navarta and Hermann 2017).

The important implication of this is that at pressures < 3 GPa, without sufficient Ti or with an excessive concentration of Na relative to Cr, only a small amount of water may actually be incorporated. Ti concentrations in olivine vary by over approximately three orders of magnitude in the upper mantle (Fig. 2). There is very little correlation with any other chemical species, although the most depleted compositions (< 5 ppm) are limited to olivine mg# > 0.92. Titanium in olivine, unlike a number of other elements, also shows an indistinct relationship with equilibration temperature (De Hoog et al. 2010), although for temperatures over 1200 °C the concentration is rarely lower than 50 ppm. Instead, Ti in olivine is most strongly correlated with bulk rock Ti, as shown through good correlations with Ti in pyroxene and garnet from the same rock (De Hoog et al. 2010). Hence the primary control on Ti in olivine will be degree of partial melting. Concentrations of both Cr and Na on the other hand show good positive correlations in upper mantle olivine with each other and also V and to a lesser extent, Al and Ca. Unlike Ti, the partitioning of these elements between mantle phases is strongly dependent on temperature, as demonstrated in natural samples by distinct relationships between concentration and equilibration temperature calculated from mineral equilibria (Witt-Eickschen and O'Neill 2005; De Hoog et al. 2010). As a result, the Cr/Na ratio in well-equilibrated upper mantle samples is relatively constant with less than an order of magnitude variation in olivine from cpx-bearing garnet and spinel peridotites (Fig. 9). Furthermore, in almost all of these mantle samples, there is a relative excess of molar Na to molar Cr. Including Li in the calculation increases the excess of molar monovalent cations (Na + Li) relative to Cr by about 15% (Table 1). This indicates that the majority of Cr³⁺ is already likely to be

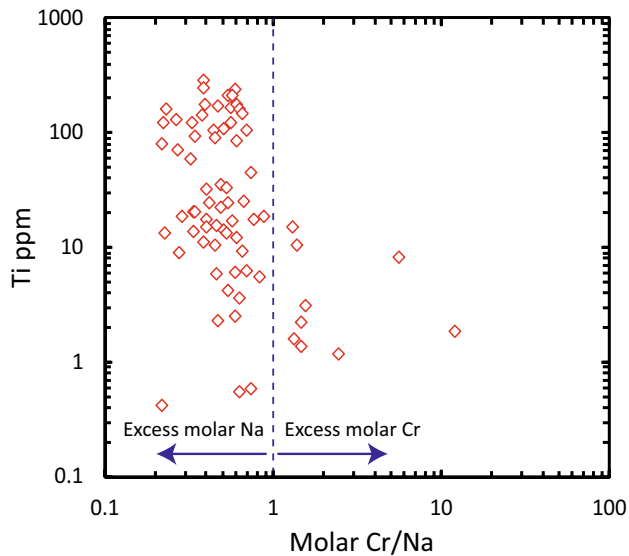


Fig. 9 Molar Cr/Na as a function of Ti concentration in well-equilibrated spinel and garnet lherzolites (De Hoog et al. 2010). A molar excess of Na limits the capacity for water to be incorporated at the [triv] point defect

charge-balanced by Na in well-equilibrated upper mantle olivine, providing an explanation as to why [triv] defects are observed so infrequently relative to [Ti] defects (e.g. Schmädicke et al. 2013). Ti concentrations on the other hand vary considerably over a small range of Cr/Na, with approximately three orders of magnitude variation for the same sample set. As a result, it is anticipated from comparison of our experimental results with the natural range of olivine trace element compositions that the availability of Ti will be the principle compositional control on water incorporation in typical upper mantle olivine at pressures < 3 GPa.

Exceptions to this, however, may be anticipated in a number of mantle settings. Of most relevance is the mantle wedge beneath volcanic arcs, since the release of water-rich fluids during subduction is the principle source of water in the upper mantle. Studies of arc mantle xenoliths indicate that sub-arc mantle is typically highly depleted relative to other mantle domains, resulting in strong depletions in moderately incompatible elements in constituent phases. Titanium in olivine from arc mantle is thus very low in concentration (< 5 ppm; Ionov 2010; Tollan et al. 2017b) and as a consequence, very low concentrations of [Ti] should be generated. This is well supported by limited FTIR data from arc mantle olivine (Soustelle et al. 2010, 2013; Tollan et al. 2015), which generally only show detectable infrared absorption at wavenumbers below 3400 cm^{-1} . Chromium however should be highly concentrated in arc mantle olivine at solidus temperatures, due to buffering by high Cr# spinel. Exceptionally low values of Cr (< 30 ppm; Ionov 2010; Tollan et al. 2017b) in arc mantle olivine are a product instead of partitioning into

pyroxene during cooling to very low sub-solidus temperatures, and thus are not truly representative of the magmatic portions of the mantle wedge. Sodium is also very low in arc mantle olivine in part due, as with Cr, to re-equilibration during cooling. Unlike Cr however, Na concentrations at solidus conditions should also be relatively low since the highly depleted, clinopyroxene-poor composition of mantle wedge peridotite means there is limited buffering potential. During hydrous metasomatism water would intuitively be anticipated to increase substantially in mantle wedge olivine, however considering the availability of trace element-related point defects, this may not be the case. Both Ti and Cr are highly depleted in subduction zone fluids, whereas Na should be strongly enriched. Metasomatism of the mantle wedge would thus maintain the low Ti concentrations in olivine, whereas the Cr/Na ratio should decrease. This increase in Na, coincidental with the increase in H_2O means that the only significant defect site available for H to occupy in pre-metasomatism arc mantle, [triv], is reduced significantly in concentration due to the competing effect of Na illustrated clearly through our study (Fig. 6). This may be compensated to some degree if this process is associated with elevated oxygen fugacity, which would lead to an increase in the proportion of Cr and Fe that is in the 3+ valance state. However, for a change in oxygen fugacity of 2 log units (Parkinson and Arculus 1999), the increase in water storage capacity is only around a factor of 2 (Bei and Kohlstedt 1993), which is a significantly smaller difference than the variation in mantle olivine Na concentration. Hence, olivine in the upper arc mantle wedge may have a very limited water storage capacity through a combination of the pre-metasomatic composition of the sub-arc mantle and the Ti, Cr-poor but Na-rich composition of hydrous slab-derived fluids.

Acknowledgements For this research was provided by an Australian Research Council Laureate Fellowship FL130100066 awarded to Hugh O'Neill. The quality of this manuscript benefited greatly from the editorial work of Hans Keppler and detailed reviews by Jed Mosenfelder and two anonymous reviewers. We would like to thank Dean Scott and David Clark for assistance with the experimental apparatus and Jonas Pape and Pierre Lanari for assistance with the microprobe measurements. Charles Le Losq and Mike Jollands are thanked for enlightening discussions.

References

- Bai Q, Kohlstedt DL (1992) Substantial hydrogen solubility in olivine and implications for water storage in the mantle. *Nature* 357(6380):672–674
- Bai Q, Kohlstedt DL (1993) Effects of chemical environment on the solubility and incorporation mechanism for hydrogen in olivine. *Phys Chem Min* 19:460–471
- Balan E, Ingrin J, Delattre S, Kovács I, Blanchard M (2011) Theoretical infrared spectrum of OH-defects in forsterite. *Eur J Miner* 23:285–292

- Balan E, Blanchard E, Lazzeri M, Ingrin J (2014) Contribution of interstitial OH groups to the incorporation of water in forsterite. *Phys Chem Min* 41:105–114
- Bali E, Bolfan-Casanova N, Koga KT (2008) Pressure and temperature dependence of H solubility in forsterite: an implication to water activity in the Earth interior. *Earth Planet Sci Lett* 268:354–363
- Batanova VG, Belousov IA, Savelieva GN, Sobolev AV (2011) Consequences of channelized and diffuse melt transport in supra-subduction zone mantle: evidence from the voykar ophiolite (Polar Urals). *J Petrol* 52:2483–2521
- Bell DR, Rossman GR, Maldener J, Endisch D, Rauch F (2003) Hydroxide in olivine: a quantitative determination of the absolute amount and calibration of the IR spectrum. *J Geophys Res.* <https://doi.org/10.1029/2001JB000679>
- Berry AJ, Hermann J, O'Neill HSTC, Foran GJ (2005) Fingerprinting the water site in mantle olivine. *Geology* 33:869–872
- Berry AJ, O'Neill HSTC, Hermann J, Scott DR (2007a) The infrared signature of water associated with trivalent cations in olivine. *Earth Planet Sci Lett* 261:134–142
- Berry AJ, Walker AM, Hermann J, O'Neill HSTC, Foran GJ, Gale JD (2007b) Titanium substitution mechanisms in forsterite. *Chem Geol* 242:176–186
- Blanchard M, Ingrin J, Balan E, Kovács I, Withers AC (2017) Effect of iron and trivalent cations on OH defects in olivine. *Am Miner* 102:302–311
- De Hoog CM, Gall L, Cornell DH (2010) Trace-element geochemistry of mantle olivine and application to mantle petrogenesis and geothermobarometry. *Chem Geol* 270:196–215
- Demouchy S, Bolfan-Casanova N (2016) Distribution and transport of hydrogen in the lithospheric mantle: a review. *Lithos* 240–243:402–425
- Demouchy S, Mackwell S (2003) Water diffusion in synthetic iron-free forsterite. *Phys Chem Miner* 30:486–494
- Demouchy S, Jacobsen SD, Fabrice G, Stern CR (2006) Rapid magma ascent recorded by water diffusion profiles in mantle olivine. *Geology* 34:429–432
- Demouchy S, Mackwell SJ, Kohlstedt DL (2007) Influence of hydrogen on Fe–Mg inter-diffusion in (Mg,Fe)O and implications for Earth's lower mantle. *Contrib Miner Petrol* 154:279–289
- Demouchy S, Thoraval C, Bolfan-Casanova N, Manthilake G (2016) Diffusivity of hydrogen in iron-bearing olivine at 3 GPa. *Phys Earth Planet Int* 260:1–13
- Denis CMM, Demouchy S, Shaw CSJ (2013) Evidence of dehydration in peridotites from Eifel Volcanic Field and estimates of the rate of magma ascent. *J Volcanol Geotherm Res* 258:85–99
- Evans TM, O'Neill HSTC, Tuff J (2008) The influence of melt composition on the partitioning of REEs, Y, Sc, Zr and Al between forsterite and melt in the system CMAS. *Geochim Cosmochim Acta* 72:5708–5721
- Faul UH, Cline IICJ, David EC, Berry AJ, Jackson I (2016) Titanium-hydroxyl defect-controlled rheology of the Earth's upper mantle. *Earth Planet Sci Lett* 452:227–237
- Férot A, Bolfan-Casanova N (2012) Water storage capacity in olivine and pyroxene to 14 GPa: Implications for the water content of the Earth's upper mantle and nature of seismic discontinuities. *Earth Planet Sci Lett* 349–350:218–230
- Gaetani GA, O'Leary JA, Shimizu N, Bucholz CE, Newville M (2012) Rapid reequilibration of H₂O and oxygen fugacity in olivine-hosted melt inclusions. *Geology* 40:915–918
- Gaetani GA, O'Leary JA, Koga KT, Hauri EH, Rose-Koga EF, Monteleone BD (2014) Hydration of mantle olivine under variable water and oxygen fugacity conditions. *Contrib Min Pet* 167:965–979
- Grant KJ, Kohn SC, Brooker RA (2007a) The partitioning of water between olivine, orthopyroxene and melt synthesised in the system albite-forsterite-H₂O. *Earth Planet Sci Lett* 260:227–241
- Grant KJ, Brooker RA, Kohn SC, Wood BJ (2007b) The effect of oxygen fugacity on hydroxyl concentrations and speciation in olivine: implications for water solubility in the upper mantle. *Earth Planet Sci Lett* 261:217–229
- Green DH, Hibberson WO, Rosenthal A, Kovács I, Yaxley GM, Fallow TJ, Brink F (2014) Experimental study of the influence of water on melting and phase assemblages in the upper mantle. *J Petrol* 55:2067–2096
- Hack AC, Mavrogenes JA (2006) A cold-sealing design for synthesis of fluid inclusions and other hydrothermal experiments in a piston-cylinder apparatus. *Am Miner* 91:203–210
- Hauri EH, Gaetani GA, Green TH (2006) Partitioning of water during melting of the Earth's upper mantle at H₂O-undersaturated conditions. *Earth Planet Sci Lett* 248:715–734
- Ingrin J, Liu J, Depecker C, Kohn SC, Balan E, Grant KJ (2013) Low-temperature evolution of OH bands in synthetic forsterite, implication for the nature of H defects at high pressure. *Phys Chem Min* 40:499–510
- Ingrin J, Kovács I, Deloule E, Balan E, Blanchard M, Kohn SC, Hermann J (2014) Identification of hydrogen defects linked to boron substitution in synthetic forsterite and natural olivine. *Am Miner* 99:2138–2141
- Ionov DA (2010) Petrology of mantle wedge lithosphere: new data on supra-subduction zone peridotite xenoliths from the andesitic Avacha volcano, Kamchatka. *J Petrol* 51:327–361
- Jochum KP, Willbold M, Raczek I, Stoll B, Herwig K (2005) Chemical characterisation of the USGS reference glasses GSA-1G, GSC-1G, GSD-1G, GSE-1G, BCR-2 and BIR-1G using EPMA, ID-TIMS, ID-ICP,MS and LA-ICP-MS. *Geostand Geoanal Res* 29:285–302
- Jochum KP, Weis U, Stoll B, Kuzmin D, Yang QC, Raczek I, Jacob DE, Stracke A, Birbaum K, Frick DA, Gunther D, Enzweiler J (2011) Determination of reference values for NIST SRM 610–617 glasses following ISO guidelines. *Geostand Geoanal Res* 35:397–429
- Jollands MC, Padrón-Navarta JA, Hermann J, O'Neill HSTC (2016) Hydrogen diffusion in Ti-doped forsterite and the preservation of metastable point defects. *Am Miner* 101:1571–1583
- Jollands MC, O'Neill HSTC, Van Orman J, Berry AJ, Hermann J, Newville M, Lanzirrotti A (2018) Substitution and diffusion of Cr²⁺ and Cr³⁺ in synthetic forsterite and natural olivine at 1200–1500 degrees C and 1 bar. *Geochim Cosmochim Acta* 220:407–428
- Kaerer B, Kalt A, Pettke T (2006) Evolution of the lithospheric mantle beneath the marsabit volcanic field (Northern Kenya): constraints from the textural, P-T and geochemical studies on xenoliths. *J Petrol* 47:2149–2184
- Karato SI (1990) The role of hydrogen diffusivity in the electrical conductivity of the upper mantle. *Nature* 347:272–273
- Kohlstedt DL, Mackwell SJ (1998) Diffusion of hydrogen and intrinsic point defects in olivine. *Z Phys Chem* 207:147–162
- Kohlstedt DL, Keppler H, Rubie DC (1996) Solubility α , β and γ phases of (Mg,Fe)₂SiO₄. *Contrib Miner Petrol* 123:345–357
- Kovács I, O'Neill HSC, Hermann J, Hauri EH (2010) Site-specific infrared OH absorption coefficients for water substitution into olivine. *Am Miner* 95:292–299
- Kovács I, Green DH, Rosenthal A, Hermann J, O'Neill HSC, Hibberson WO, Udvardi B (2012) An experimental study of water in nominally anhydrous minerals in the upper mantle near the water-saturated solidus. *J Petrol* 53:2067–2093
- Lemaire C, Kohn SC, Brooker RA (2004) The effect of silica activity on the incorporation mechanisms of water in synthetic forsterite: a polarised infrared spectroscopic study. *Contrib Miner Petrol* 147:48–57
- Mackwell SJ, Kohlstedt DL, Paterson MS (1985) The role of water in the deformation of olivine single crystals. *J Geophys Res* 90:11319–11311

- Mackwell SJ, Kohlstedt DL (1990) Diffusion of hydrogen in olivine: implications for water in the mantle. *J Geophys Res* 95:5079–5088
- Matsyuk SS, Langer K (2004) Hydroxyl in olivines from mantle xenoliths in kimberlites of the Siberian platform. *Contrib Miner Petrol* 147:413–437
- Matveev S, O'Neill HSTC, Ballhaus C, Taylor WR, Green DH (2001) Effect of silica activity on OH⁻ IR spectra of olivine: implications for low-*a*SiO₂ mantle metasomatism. *J Petrol* 42:721–729
- Mei S, Kohlstedt DL (2000) Influence of water on plastic deformation of olivine aggregates 1. Diffusion creep regime. *J Geophys Res* 105:21457–21469
- Miller GH, Rossman GR, Harlow GE (1987) The natural occurrence of hydroxide in olivine. *Phys Chem Min* 14:461–472
- Mosenfelder JL, Deligne NI, Asmiow PAD, Rossman GR (2006) Hydrogen incorporation in olivine from 2 to 12 GPa. *Am Miner* 91:285–294
- Mosenfelder JL, Le Vozer M, Rossman GR, Guan Y, Bell DR, Asimow PD, Eiler JM (2011) Analysis of hydrogen in olivine by SIMS: evaluation of standards and protocol. *Am Miner* 96:1725–1741
- Neumann E-R, Griffin WL, Pearson NJ, O'Reilly SY (2004) The evolution of the upper mantle beneath the Canary Islands: information from trace elements and Sr isotope ratios in minerals in mantle xenoliths. *J Petrol* 45:2573–2612
- Niida K, Green DH (1999) Stability and chemical composition of pargasitic amphibole in MORB pyroxene under upper mantle conditions. *Contrib Miner Petrol* 135:18–40
- Padrón-Navarta JA, Hermann J (2017) A subsolidus olivine water solubility equation for the earth's upper mantle. *J Geophys Res* 122:9862–9880
- Padrón-Navarta JA, Hermann J, O'Neill HSTC (2014) Site-specific hydrogen diffusion rates in forsterite. *Earth Planet Sci Lett* 392:100–112
- Parkinson IJ, Arculus RJ (1999) The redox state of subduction zones: insights from arc-peridotites. *Chem Geol* 160:409–423
- Peslier AH, Luhr JF (2006) Hydrogen loss from olivines in mantle xenoliths from Simcoe (USA) and Mexico: Mafic alkalic magma ascent rates and water budget of the sub-continental lithosphere. *Earth Planet Sci Lett* 242:302–319
- Peslier AH, Woodland AB, Wolff JA (2008) Fast kimberlite ascent rates estimated from hydrogen diffusion profiles in xenolithic mantle olivines from southern Africa. *Geochim Cosmochim Acta* 72:2711–2722
- Peslier AH, Woodland AB, Bell DR, Lazarov M (2010) Olivine water contents in the continental lithosphere and the longevity of cratons. *Nature* 467:78–81
- Pirard C, Hermann J, O'Neill HSTC (2013) Petrology and geochemistry of the crust-mantle boundary in a Nascent Arc, Massif du Sud Ophiolite, New Caledonia, SW Pacific. *J Petrol* 54:1759–1792
- Pitzer KS, Sterner SM (1994) Equations of state valid continuously from zero to extreme pressures for H₂O and CO₂. *J Chem Phys* 101:3111–3116
- Qin T, Wentzcovitch RM, Umemoto K, Hirschmann MM, Kohlstedt DL (2018) Ab initio study of water speciation in forsterite: importance of the entropic effect. *Am Miner* 103:692–699
- Schmädicke E, Gose J, Witt-Eickschen G, Brätz H (2013) Olivine from spinel peridotite xenoliths: hydroxyl incorporation and mineral composition. *Am Miner* 98:1870–1880
- Shen T, Hermann J, Zhang L, Padrón-Navarta JA, Chen J (2014) FTIR spectroscopy of Ti-chondrodite, Ti-clinohumite, and olivine in deeply subducted serpentinites and implications for the deep water cycle. *Contrib Miner Petrol* 167:992–1007
- Smith D (2013) Olivine thermometry and source constraints for mantle fragments in the Navajo Volcanic Field, Colorado Plateau, southwest United States: implications for the Mantle Wedge. *Geochem Geophys Geosyst*. <https://doi.org/10.1002/ggge.20065>
- Smyth JR, Frost DJ, Nestola F, Holl CM, Bromiley G (2006) Olivine hydration in the deep upper mantle: effects of temperature and silica activity. *Geophys Res Lett* 33:L15301
- Soustelle V, Tommasi A, Demouchy S, Ionov DA (2010) Deformation and fluid-rock interaction in the supra-subduction mantle: microstructures and water contents in peridotite xenoliths from the Avacha Volcano, Kamchatka. *J Petrol* 51:363–394
- Soustelle V, Tommasi A, Demouchy S, Franz L (2013) Melt-rock interactions, deformation, hydration and seismic properties in the sub-arc lithospheric mantle inferred from xenoliths from seamounts near Lihir, Papua New Guinea. *Tectonophysics* 608:330–345
- Spandler C, O'Neill HSTC (2010) Diffusion and partition coefficients of minor and trace elements in San Carlos olivine at 1300 °C with some geochemical implications. *Contrib Miner Petrol* 159:791–818
- Tollan PME, O'Neill HSTC, Hermann J, Benedictus A, Arculus RJ (2015) Frozen melt-rock reaction in a peridotite xenolith from sub-arc mantle recorded by diffusion of trace elements and water in olivine. *Earth Planet Sci Lett* 422:169–181
- Tollan PME, Smith R, O'Neill HSTC, Hermann J (2017a) The responses of the four main substitution mechanisms of H in olivine to H₂O activity at 1050 °C and 3 GPa. *Prog Earth Planet Sci* 4:14–34
- Tollan PME, Dale CW, Hermann J, Davidson JP, Arculus RJ (2017b) Generation and modification of the mantle wedge and lithosphere beneath the west bismarck island arc: melting, metasomatism and thermal history of peridotite xenoliths from Ritter Island. *J Petrol* 58:1475–1510
- Umemoto K, Wentzcovitch RM, Hirschmann M, Kohlstedt DL, Withers AC (2011) A first-principles investigation of hydrous defects and IR frequencies in forsterite: the case for Si vacancies. *Am Miner* 96:1475–1479
- Walker AM, Hermann J, Berry AJ, O'Neill HSTC (2007) Three water sites in upper mantle olivine and the role of titanium in the water weakening mechanism. *J Geophys Res* 112:B05211
- Wanamaker BJ (1994) Point defect diffusivities in San Carlos olivine derived from reequilibration of electrical conductivity following changes in oxygen fugacity. *Geophys Res Lett* 21:21–24
- Wang ZY, Hiraga T, Kohlstedt DL (2004) Effect of H⁺ on Fe–Mg interdiffusion in olivine. (Fe,Mg)₂SiO₄. *App Phys Lett* 85:209–211
- Wilshire HG, Shervais JW (1975) Al-augite and Cr-diopside ultramafic xenoliths in basaltic rocks from western United States. *Phys Chem Earth* 9:257–272
- Withers AC, Hirschmann MM (2008) Influence of temperature, composition, silica activity and oxygen fugacity on the H₂O storage capacity of olivine at 8 GPa. *Contrib Miner Petrol* 165:595–605
- Withers AC, Hirschmann MM, Tenner TJ (2011) The effect of Fe on olivine H₂O storage capacity: consequences for H₂O in the martian mantle. *Am Miner* 96:1039–1053
- Withers AC, Bureau H, Raepsaet C, Hirschmann MM (2012) Calibration of infrared spectroscopy by elastic recoil detection analysis of H in synthetic olivine. *Chem Geol* 334:92–98
- Witt-Eickschen G, O'Neill HSTC (2005) The effect of temperature on the equilibrium distribution of trace elements between clinopyroxene, orthopyroxene, olivine and spinel in upper mantle peridotite. *Chem Geol* 221:65–101
- Yang X (2016) Effect of oxygen fugacity on OH dissolution in olivine under peridotite-saturated conditions: an experimental study at 1.5–7 GPa and 1100–1300 °C. *Geochim Cosmochim* 173:319–336
- Yoshino T, Matsuzaki T, Yamashita S, Katsura T (2006) Hydrous olivine unable to account for conductivity anomaly at the top of the asthenosphere. *Nature* 443:973–976
- Zhao Y-H, Ginsberg SB, Kohlstedt DL (2004) Solubility of hydrogen in olivine: dependence on temperature and iron content. *Contrib Miner Petrol* 147:155–161
- Zheng JP, Zhang RY, Griffin WL, Liou JG, O'Reilly SY (2005) Heterogeneous and metasomatized mantle recorded by trace elements

- in minerals of the Donghai garnet peridotites, Sulu UHP terrane, China. *Chem Geol* 221:243–259
- Zheng JP, Griffin WL, O'Reilly SY, Yu CM, Zhang HF, Pearson N, Zhang M (2007) Mechanism and timing of lithospheric modification and replacement beneath the eastern North China Craton: peridotitic xenoliths from the 100 Ma Fuxin basalts and a regional synthesis. *Geochim Cosmochim Acta* 71:5203–5225
- Zhukova I, O'Neill HSC, Campbell IH (2017) A subsidiary fast-diffusing substitution mechanism of Al in forsterite investigated using diffusion experiments under controlled thermodynamic conditions. *Contrib Miner Petrol* 172:53–65